International Journal of Impact Engineering 182 (2023) 104768

Contents lists available at ScienceDirect

International Journal of Impact Engineering

journal homepage: www.elsevier.com/locate/ijimpeng

# A novel analytical framework for assessing the impact response of SFRC beam

Mohammad Bakhshi [a,*], Joaquim A.O. Barros [a], Mohammadali Rezazadeh [b], Isabel B. Valente [a], Honeyeh Ramezansefat [a]

[a] Department of Civil Engineering, Faculty of Engineering, University of Minho, Guimaraes, Portugal
[b] Department of Mechanical and Construction Engineering, Northumbria University, Newcastle-upon-Tyne, England

ARTICLE INFO

*Keywords:*
Analytical model
Steel fiber reinforced concrete
Energy balance
Strain rate
Drop weight test
Concrete beam

ABSTRACT

This paper presents a novel model for predicting the impact response of steel fiber reinforced concrete (SFRC) beams. The model utilizes the principles of energy conservation and impulse-momentum theorem to calculate the maximum reaction force and peak impact force. A tensile behavior model for simulating the concrete behavior is proposed considering the effect of volume fraction of steel fibers and the effect of strain rate on the concrete properties. Additionally, the conventional beam theory, along with a cross-section-layered approach, is used to express the total beam's reaction forces vs deflection relationship. Afterwards, the model calculates the maximum midspan deflection of SFRC beams subjected to impact loading by applying the principle of conservation of energy and considering the effect of strain rate. The proposed model is compared with 121 impact tests, and the results show that the model can estimate the maximum reaction force of SFRC beams with acceptable accuracy.

## 1. Introduction

Concrete is one of the most applied materials in structural constructions. The addition of fibers to plain concrete can reduce its brittle behavior [1]. By designing a proper mix composition for mobilizing effectively the fiber reinforcement mechanisms, the maximum concrete crack width can decrease significantly, because the fibers have increased the post-cracking tensile capacity provided by the fibers [2]. Over the past decades, steel fibers have been utilized as a reinforcement system to ameliorate the mechanical characteristics and durability of structural elements, when tension and shear dominate their failure modes [3], as occurs in beams. The higher shear capacity of steel fiber reinforced concrete (SFRC) beams over their corresponding non-fibrous reference beams, is due to the fibers pullout mechanisms, bridging the shear cracks caused by the applied shear force. Restraining the relative movement of these crack faces also enhances the aggregate interlock shear-resisting mechanisms. Finally, by offering resistance to crack propagation, fibers ensure a higher volume of uncracked concrete subjected to compression that contributes to the beam's shear capacity, [4–6]. These advantages of fiber addition in the concrete mixture can be seen in the post-cracking tensile capacity, impact resistance, and toughness, but in current applications, the fiber content has a minimal effect on the compressive strength [7–9].

In contrast, mechanical properties of concrete are influenced by the strain rate applied during loading, [1]. Concrete responds differently to varying strain rates depending on the type of loading, whether it's compressive, tensile, or flexural, [6–12]. The dynamic increase factor (DIF) is commonly used to characterize the strain rate dependence of concrete materials, [4–6]. DIF of a certain material property is the ratio of its dynamic to quasi-static values. Studies conducted on the dynamic behavior of SFRC have demonstrated that higher loading strain rates lead to an increase in both the tensile strength and mode-I fracture energy, [13–22]. Consequently, both tensile and flexural behavior of concrete are rate dependent parameters. These properties affect significantly the flexural behavior of SFRC beams, [23]. Accordingly, the energy absorption capacity and the reaction force of SFRC beams are also strain rate dependent. In SFRC beams subjected to impact loading, part of the overall energy applied by the impactor is absorbed by the beam's deformational capacity, while the rest is spent by the internal work produced by an applied stress field during the deformation of the corresponding body (due to the beam's acceleration motion under impact loading), [24–26]. Therefore, in a simply supported beam subjected to impact loading, the total force exerted by the impactor is equal

* Corresponding author.
*E-mail address:* id8290@alunos.uminho.pt (M. Bakhshi).

https://doi.org/10.1016/j.ijimpeng.2023.104768
Received 1 April 2023; Received in revised form 28 July 2023; Accepted 28 August 2023
Available online 30 August 2023

**List of symbols and abbreviations**

*Abbreviations*

| | |
|---|---|
| DIF | Dynamic increase factor |
| FRC | Fiber reinforced concrete |
| ITZ | Interfacial transition zone and mean |
| MAD | Mean absolute deviation |
| MAPE | Mean absolute percentage error |
| SFRC | Steel fiber reinforced concrete |

*Symbols*

| | |
|---|---|
| $A$ | Beam's cross-section area [$m^2$] |
| $exp$ | Experimental results |
| $E$ | Concrete modulus of elasticity [MPa] |
| $E_{c,dy}$ | Dynamic modulus of elasticity [MPa] |
| $E_P$ | Initial potential energy [J] |
| $E_{cap.}$ | Energy absorption capacity of the beam [J] |
| $E_k$ | Initial kinetic energy [J] |
| $E_{max}$ | Energy absorbed by the beam up to $\delta_{max}$ [J] |
| $E_{k,cr}$ | Critical kinetic energy [J] |
| $E_k^{'}$ | Kinetic energy of impactor at the moment of failure [J] |
| $f_{cm}$ | Static compressive strength [MPa] |
| $f_{cm,dy}$ | Dynamic compressive strength [MPa] |
| $f_{ctm,dy}$ | Dynamic tensile strength [MPa] |
| $g$ | Gravity acceleration [$m/s^2$] |
| $G_{Ff}$ | Static fracture energy [N/m] |
| $G_{F,dy}$ | Dynamic fracture energy [N/m] |
| $g_{Ff}$ | Static fracture energy density [MPa] |
| $g_{Ff,dy}$ | Dynamic fracture energy density [MPa] |
| $H$ | Height of impactor [m] |
| $I$ | Inertia moment of beam's cross-section [$m^4$] |
| $k$ | Linear flexural stiffness of the beam [N/m] |
| $l$ | Beam's length [m] |
| $l_b$ | Characteristic length [m] |
| $m$ | Impactor mass [kg] |
| $m^{'}$ | Mass of the beam [kg] |
| $M$ | Beam's bending moment [N.m] |
| $M_{un}$ | Bending moment due to a unit load configuration [N.m] |
| $M_l$ | Bending moment due to a real load configuration [N.m] |
| $M_{peak}$ | Peak moment [N.m] |
| $N$ | Total number of specimens |
| $pre$ | Model predictions |
| $P_b$ | Total reaction forces in the supports [N] |
| $P_{b,peak}$ | Peak reaction forces [N] |
| $P_i$ | Total inertia force [N] |
| $P_t$ | Impact force [N] |
| $p_{i,mid}$ | Inertia forces at the beam's midspan [N/m] |
| $p_{i,end}$ | Inertia forces at ends of the beam [N/m] |
| $\Delta P$ | Impulse variation [kg.m/s] |
| $s$ | Beam's overhanging length [m] |
| $t_p$ | Time interval of the impact load [s] |
| $V_c$ | Initial contact velocity [m/s] |
| $V_{peak}$ | Peak shear force [N] |
| $V_s$ | Velocity of SFRC beam and impactor after collision [m/s] |
| $V^{'}$ | Velocity of the impactor at the moment of failure [m/s] |
| $V(x)$ | Shear force during beam's length [N] |
| $W_f$ | Fiber weight percentage [%] |
| $\gamma$ | Shear strain |
| $\delta_m$ | Deflection due to bending [m] |
| $\delta_{max}$ | Maximum midspan deflection [m] |
| $\delta_{peak}$ | Peak deflection at beam's midspan [m] |
| $\delta_u$ | Ultimate deflection at beam's midspan [m] |
| $\delta_v$ | Deflection due to shear [m] |
| $\dot{\delta}_d$ | Dynamic midspan displacement rate [m/s] |
| $\ddot{\delta}$ | Beam's midspan acceleration [$m/s^2$] |
| $\ddot{\delta}_{max}$ | Maximum midspan acceleration [$m/s^2$] |
| $\varepsilon_{cr}$ | Strain at static tensile strength |
| $\varepsilon_{cl}$ | Strain at peak stress |
| $\dot{\varepsilon}_c$ | Compressive strain rate [1/s] |
| $\dot{\varepsilon}_t$ | Tensile strain rate [1/s] |
| $\rho$ | Density of SFRC [$kg/m^3$] |
| $\chi$ | Beam's curvature [1/m] |
| $\psi$ | Total inertia force to impact force ratio |
| $\omega$ | Predicted to experimental peak impact force ratio |

to the sum of the total inertia forces and reaction forces acting on the beam's supports. The impact force that causes the beam's failure is defined as the impact strength capacity of the SFRC beam, [27,28]. It should be noted that a time delay exists between the reaction force responses and the impact force, due to the time taken by the shear stress wave to travel from the impact loading point to the beam's supports [23,29]. This implies that, during the time delay, the supports do not sense any loads, and the beam is effectively subjected to a one-point load at its midspan. However, since this time delay depends on the geometrical properties of elements and is relatively small compared to the total impact loading time [11,13,28], the test process is simulated assuming a three-point bending test by ignoring the time delay, aiming to avoid more complexity in the model.

Experimental research on the flexural behavior of SFRC beams under impact load has faced some advances in the past, but due to the complex phenomena involving the simulation of this behavior, analytical models are still scarce. In an effort to predict the behavior of SFRC beams subjected to drop-weight impact, an analytical model was established based on the energy conservation law, [24]. According to the kinetic energy of the impactor, the SFRC beam can develop the following types of response: (a) completely fails and separates into two segments and may have some residual kinetic energy after it fractures [11,13,23]; (b) absorbs the kinetic energy of impactor without failure, [14]. At the point of complete failure of SFRC beams under impact loading, the total reaction forces and inertia force are equivalent to the SFRC beams' impact strength capacity. This indicates that the minimum initial energy required to fracture the SFRC beam is equivalent to the sum of the potential energy generated by the beam's deflection and the energy absorbed by the beam (calculated by the area under the SFRC beam's reaction force-deflection diagram). As a result, a critical kinetic energy value of the impactor can be defined for every SFRC beam, which is dependent on the beam's energy absorption capacity. When SFRC beams absorb the total energy of the impactor without failure, the impact force-deflection diagram is predictable, and accordingly, the maximum reaction force of the beam can be obtained.

The present paper proposes a practical innovative model with a design framework that can be used to predict both the maximum midspan deflection and the peak impact force of simply supported SFRC beams subjected to impact loading. The existing inertia effect during the impact process, often ignored in the literature, is considered in this paper. Although the inertia force can be ignored in calculating the reaction force, it must be predicted to obtain the impact force (applied by the impactor). In the present research, an analytical model is proposed to predict the maximum acceleration, inertia force and corresponding moment and shear force distribution along the beam. Then, a strain rate-dependent constitutive model to predict the impact force-deflection

relation of the SFRC beam is derived. Accordingly, an energy-balanced approach is proposed to determine the maximum impact force. Finally, the predictive performance of the proposed model is appraised by using experimental results of 121 SFRC beams tested under drop-weight impact loads.

## 2. Proposed analytical model

Due to the existing acceleration caused by dynamic loading at the beam's midspan, the behavior of the beams under quasi-static and dynamic loading are different. Therefore, the maximum acceleration at the beam's midspan is an effective parameter to analyze its flexural behavior. In order to calculate the maximum acceleration, a statistical analysis is performed, and a simplified model is suggested, based on the available experimental results, [17]. Then, according to the mechanical characteristics of the concrete and geometry of the beam, a model is proposed to predict the maximum impact force at the midspan. The model is clearly explained through a flowchart (in Section 2.2). The predictive performance of a model for determining the beam's total reaction forces-deflection diagram subjected to the impact loading depends on the accuracy of the models used for simulating the compressive and tensile behavior of SFRCs under different strain rates. Hence, a focus is given in these aspects. Finally, considering the moment-curvature diagram obtained based from a layered-section approach, the SFRC beam geometry and using the unit-load method, the force-deflection diagram is obtained.

### 2.1. Dynamic response of a SFRC beam under an impact load

When a beam is subjected to impact loading, acceleration is generated, and this causes an inertia force to develop along the beam. The direction of the inertia force is opposite to the direction of the beam's movement. Consequently, unlike the beam under static loading, the impact force, $P_t$, on a simply supported beam is equal to the summation of the reaction forces in the supports, $P_b = R_1 + R_2$, and the total inertia forces, $P_i$, Eq. (1).

$$P_t = P_i + P_b \tag{1}$$

The total inertia force (total area under inertia force distribution), $P_i$ Eq. (2)), is function of acceleration ($\ddot{\delta}$), density of materials ($\rho$), and beam's cross-section area ($A$). The results derived experiments conducted on fiber-reinforced concrete (FRC) elements are supporting the assumption considered by Bentur et al. [17] which states that the accelerations and displacements along the beam's length are distributed linearly, see Eq. (2). Hence, the value of inertia forces at the midspan, $p_{i,mid}$, and at the ends of the beam, $p_{i,end}$, are calculated based on the geometry of the beam, Eqs. (3) and ((4).

$$P_i = \rho A \ddot{\delta}_{max}\left[\frac{l}{3} + \frac{8}{3}\frac{s^3}{l^2}\right] \tag{2}$$

$$p_{i,mid} = \frac{2lP_i}{l^2 - 4s^2} \tag{3}$$

$$p_{i,end} = \frac{4sP_i}{l^2 - 4s^2} \tag{4}$$

where $l$ and $s$ are the beam's length and overhanging length, respectively, as shown in Fig. 1. Based on the assumed linear inertia force distribution along the beam [17] and the load applied by the impactor, shear force and moment distribution along the beam can be obtained from Eqs. (5a) and (5b).

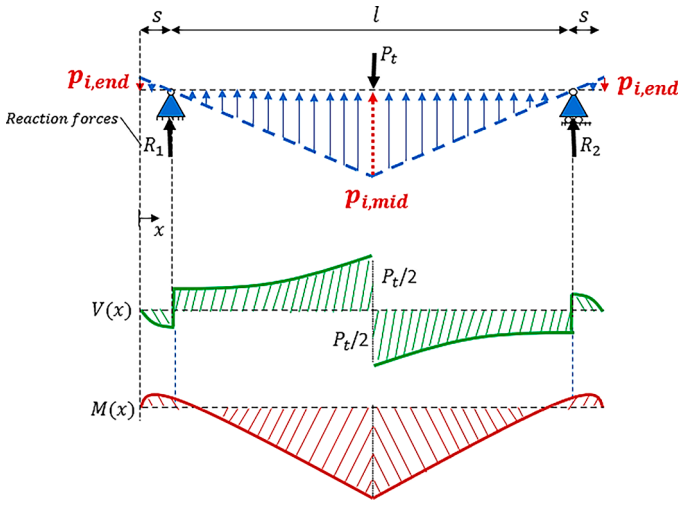


**Fig. 1.** Shear, bending moment, and loading diagrams for a beam under an impact loading.

$$V(x) = \begin{cases} \left(\frac{2\psi P_t}{l^2 - 4s^2}\right)(x^2 - 2sx), & 0 \le x < s \\ \left(\frac{2\psi P_t}{l^2 - 4s^2}\right)(x^2 - 2sx) + \left(\frac{(1-\psi)P_t}{2}\right), & s \le x \le s + \frac{l}{2} \end{cases} \tag{5a}$$

$$M = \begin{cases} \left[\frac{2\psi P_t}{3(l^2 - 4s^2)}\right](x^3 - 3sx^2), & 0 \le x < s \\ \left[\frac{2\psi P_t}{3(l^2 - 4s^2)}\right](x^3 - 3sx^2) + \left[\frac{(1-\psi)P_t}{2}\right](x - s), & s \le x \le s + \frac{l}{2} \end{cases} \tag{5b}$$

$$\psi = \frac{P_i}{P_t} = \frac{P_i}{P_i + P_b} \tag{6}$$

The maximum midspan acceleration of the beam is, in general, dependent on the height and mass of impactor, beam geometry, and materials properties, [9]. To predict accurately the maximum midspan acceleration, a model must include the abovementioned parameters. The linear flexural stiffness of a simply supported beam, $48EI/l^3$, was considered as representative, where $E$ and $I$ are the concrete modulus of elasticity and the inertia moment of the beam's cross-section, respectively. Due to the limited experimental data, shear stiffness of the beam is ignored in proposing a model of maximum midspan acceleration. Based on the available experimental results conducted by Banthia et al. [9], the present research performs a statistical analysis to investigate the effect of the following input variables: beam stiffness, height and mass of the impactor, on the maximum beam's midspan acceleration. After further statistical processing to clean data from incorrect or incomplete records with missing information on important variables, the database was limited to 33 simply supported beams tested under impact loading. According to this database, the statistical P-value of the mass of the impactor is more than 0.05, which means that the mass of the impactor has a negligible effect on the maximum acceleration at the beam's midspan. The closer to zero is the P-value, the more significant is the variable from the statistical point of view, i.e., the effect of dependent parameters on the independent parameter is stronger. Additionally, since the data does not have much variation in input variables, the beam flexural stiffness and the height of the impactor were considered as categorical input variables instead of continuous input variables. Considering the limited availability of studies in this particular field, the classifications were performed using statistical calculations in order to achieve a reasonable level of accuracy. To achieve almost the same

amount of data in each category, the beam stiffness was divided into three groups, while the height of the impactor was divided into four groups, Table 1. This division was done to ensure that each category contained a similar amount of data, thereby maintaining a balanced distribution. According to this organization of the input data, if data is placed in any of the categories, each group of data has a specific number that indicates their effectiveness. For example, for the height of the impactor, if the data is in the first category, the value of $H_1$ is equal to one (effective), while the value of $H_2$, $H_3$, and $H_4$ are zero (ineffective). In the performed statistical analysis, a linear regression was adopted, and the results obtained are presented in Table 2.

Finally, based on the five input variables (three groups of the height of impactor, $H_2$, $H_3$, and $H_4$, and two groups of the beam's flexural stiffness, $k_2$ and $k_3$), a curve fitting of the maximum midspan acceleration, $\ddot{\delta}_{max}$, recorded in the experimental tests with SFRC beams was derived (as shown in Fig. 2). Eq. (7) was obtained by employing the statistical approach of the least-squares method to determine the optimal match for a collection of data points through the reduction of the overall sum of discrepancies or residuals from the fitted curve. The correlation coefficient is 88%. The maximum midspan acceleration is utilized to calculate the maximum inertia force during the loading. It must be noted that the maximum acceleration in this relationship is calculated in terms of $g = 9.81\ m.s^{-2}$,

$$\ddot{\delta}_{max}[g] = 691.4 + 85.5H_2 + 373.4H_3 + 548.1H_4 - 78.4k_2 - 289.3k_3 \quad (7)$$

where the values of $H_2$, $H_3$, $H_4$, $k_2$ and $k_3$ are shown in Table 1. The present linear regression model, Table 2, includes a constant called the regression intercept and three estimating regression coefficients that show the effect of each dependent variable ($H_2$, $H_3$, $H_4$, $k_2$ and $k_3$) on the independent variable ($\ddot{\delta}_{max}$). The standard error of the mean is an estimate of a parameter that indicates how different the total mean is likely to be from a sample mean. The confidence interval of 95% on the mean for each variable is shown, which indicates that the estimated mean falls within the range of 95% of the results. The variables of $H_1$ and $k_1$ are considered the base parameters of the categorical data. It means that the constant value of 691.4 is for the condition where $H_1$ and $k_1$ are equal to one and the values of $H_2$, $H_3$, $H_4$, $k_2$ and $k_3$ are null. According to the proposed model, the beam's acceleration increases with the height of the impactor (positive coefficients) and decreases with the beam's stiffness (negative coefficients).

The effect of these two categorical parameters ($H$ and $k$) on the maximum beam's midspan acceleration, by using Eq. (7), can be reasonably justified by the deformational response of a beam under the applied impact loading process., Failure of SFRC elements can be abrupt due to a lack of efficiency of fiber reinforcement mechanisms in wide cracks, because the fiber reinforcement has a discrete nature and, generally, a relatively small content of fibers is used in real applications. After collision, during impact loading, the SFRC beam and impactor will have the same velocity, $V_s$ (see Fig. 3c), which is dependent on the initial contact velocity, $V_c$ (see Fig. 3b), [27]. It should be noted that the horizontal velocities and acceleration was ignored during impact process. On the other hand, the initial contact velocity (or height of the impactor) can be considered as one of the parameters with higher influence on the beam's acceleration. By raising the contact velocity, the velocity difference before and after collision increases. The strain rate effects on the beam's behavior increases with the contact velocity due to the alterations of the material properties and leads to an increase in compressive and tensile strengths of the SFRC beam. Consequently, the energy absorption capacity of the beam would be higher and the velocity after collision does not necessarily increase. In addition, since the concrete brittleness increases with the beam's stiffness, the energy absorption capacity of SFRC beam also decreases with the beam's stiffness. Therefore, by increasing the beam's stiffness, the velocity difference before and after collision decreases. Moreover, based on the conservation of energy law, the contact velocity of the impactor is independent from its mass, $m$. As a result, both the height of the impactor ($H$) and the stiffness of the SFRC beam are effective parameters for the maximum midspan acceleration [30].

The sensitivity analysis on the height of the impactor and on the stiffness of the beam is illustrated in Fig. 4 which is based on Eq. (7). For evaluating the effect of $H$ and $k$ on the maximum midspan acceleration separately, the null values of $k_2$ and $k_3$ (for $H$) and $H_2$, $H_3$, and $H_4$ (for $k$) are considered, respectively. As shown in Fig. 4, $\ddot{\delta}_{max}$ increases with $H$, and decreases with the beam's stiffness. The obtained results support the existence of three categories for the effect of the height of the impactor and two categories for the effect of the beam's flexural stiffness.

**Table 1**
Categorical data for the adopted variables.

| Variables | Categorical type |
|---|---|
| $k \leq 2.5E+07\ N.m^{-1}$ | $k_1 = 1;\ k_2 = 0;\ k_3 = 0$ |
| $2.5E+07\ N.m^{-1} < k \leq 3.5E+07\ N.m^{-1}$ | $k_1 = 0;\ k_2 = 1;\ k_3 = 0$ |
| $k > 3.5E+07\ N.m^{-1}$ | $k_1 = 0;\ k_2 = 0;\ k_3 = 1$ |
| $H \leq 0.2\,m$ | $H_1 = 1;\ H_2 = 0;\ H_3 = 0;\ H_4 = 0$ |
| $0.2\,m < H \leq 0.4\,m$ | $H_1 = 0;\ H_2 = 1;\ H_3 = 0;\ H_4 = 0$ |
| $0.4\,m < H \leq 0.6\,m$ | $H_1 = 0;\ H_2 = 0;\ H_3 = 1;\ H_4 = 0$ |
| $H > 0.6\,m$ | $H_1 = 0;\ H_2 = 0;\ H_3 = 0;\ H_4 = 1$ |

### 2.2. Energy-balance based model

The energy-balance model is a frequently employed method for predicting impact force [24,27]. During the impact event, the initial kinetic energy of the impactor, $E_k$, results in the deformation of the beam. As shown in Fig. 5, for a SFRC beam under the dropping down of an impactor the energy balance equation is defined as the equality of the initial kinetic energy of impactor before collision and total energy absorbed by SFRC beam and the kinetic energy of impactor after collision (in case of SFRC fracture). The impact model is developed assuming SFRC beams subjected to symmetric impact loading conditions without any rotational movement of the beams, as the relevant experimental studies in the literature did not monitor or report these rotational movements during the impact loading tests. However, it was evidenced that for the symmetric loading conditions, the contribution of possible rotational energy to overall dynamic behavior of element is relatively small compared to other effective factors [30,31]. Therefore, the minimized effect of rotational energy is assumed during the impact process. Energy absorption capacity of the beam, $E_{cap.}$, is obtained by integrating the beam's force ($P_b$)-deflection response ($f(\delta)$), see Eq. (8), where $P_b$ is the total reaction. The evaluation of $f(\delta)$ will be treated in Section 2.3 by considering the flexural and shear stiffness of the beam.

The initial potential energy, $E_P$, of the impactor at the specified height, $H$, is converted into the initial kinetic energy, $E_k$, at its contact moment with the beam. This condition is represented by Eq. (9b), from which it can be obtained the initial contact velocity, $V_c$, Eq. (9b), where $m$ and $g$ are the mass of the impactor and the gravity acceleration and, respectively.

$$E_{cap.} = \int_0^{\delta_u} f(\delta)d\delta \quad (8)$$

$$E_k = E_P \quad \rightarrow \quad 0.5mV_c^2 = mgH \quad (9a)$$

$$V_c = \sqrt{2gH} \quad (9b)$$

As mentioned previously, there are two scenarios regarding the SFRC beam behavior under impact loading. In one scenario, it is assumed that the SFRC beam does not fail abruptly during impact loading, i.e., it deforms up to its maximum deflection, $\delta_{max}$, when the impactor's velocity reaches zero, and, consequently, all initial kinetic energy is dissipated by deforming the beam. In the other scenario, the SFRC beam

**Table 2**
Summary output of regression statistics.

| Variables | | Coefficients | Standard Error | P-value | Lower 95% | Upper 95% |
|---|---|---|---|---|---|---|
| Intercept | | 691.401 | 60.184 | 6.7E-12 | 567.912 | 814.809 |
| The beam's stiffness, $k$ ($N.m^{-1}$) | $k_1$ | Base parameter of the categorical data | | | | |
| | $k_2$ | −78.381 | 67.217 | 2.5E-03 | −216.301 | 59.538 |
| | $k_3$ | −289.331 | 62.825 | 8.8E-05 | −418.238 | −160.422 |
| The height of the impactor, $H$ ($m$) | $H_1$ | Base parameter of the categorical data | | | | |
| | $H_2$ | 85.511 | 73.976 | 2.5E-02 | −66.276 | 237.299 |
| | $H_3$ | 373.356 | 64.913 | 4.1E-06 | 240.165 | 506.547 |
| | $H_4$ | 548.052 | 99.099 | 7.2E-06 | 344.901 | 751.203 |

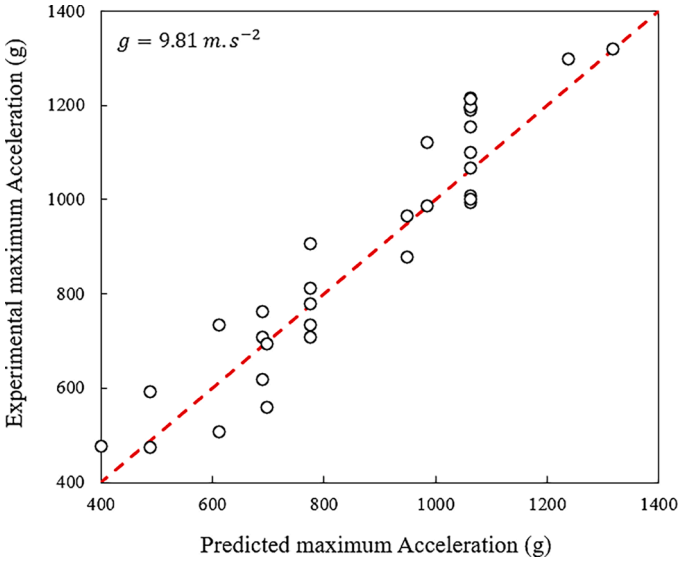


**Fig. 2.** Comparison of maximum beam's midspan acceleration registered experimentally and estimated statistically.

is assumed to completely fracture, thereby after the collision between the impactor and beam, the impactor passes through the beam. The impactor's kinetic energy after the collision is dependent on its initial kinetic energy before the collision and the energy absorption capacity of the beam, ignoring the effect of rotational energy during impact process. Consequently, to define these two scenarios, a critical kinetic energy, $E_{k,cr}$, is proposed, as being the maximum initial kinetic energy that the beam can absorb up to its failure. In other words, $E_{k,cr}$ is the minimum amount of energy to completely fracture the SFRC beam, which is determined from the energy balance equation:

$$E_{k,cr} + E_{p,\ def.} = E_{cap.} \tag{10}$$

$$E_{k,cr} = E_{cap.} - E_{p,\ def.} = \int_0^{\delta_u} f(\delta)d\delta - (m+m')g\delta_u \tag{11a}$$

$$m' = \rho bh(l+2s) \tag{11b}$$

where $E_{p,\ def.}$ is the potential energy resulting from the deflection of the beam, Fig. 5. In Eq. (11b) $\delta_u$ and $m'$ are the ultimate deflection and the mass of the beam, respectively. This equation shows that the critical kinetic energy, $E_{k,cr}$, depends on the mass of the beam and impactor, as well as on the energy absorption capacity of the SFRC beam up to its ultimate deflection. Considering the effect of the strain rate on the SFRC properties (tensile and compressive behavior), the flexural behavior of the SFRC beam can be predicted for beams with different geometries. The strain rate effects introduced in the beam depend on the initial collision velocity induced by impactor height. Therefore, the change in the initial height of the impactor causes a change in the behavior of the SFRC, which in turn changes the beam's bearing capacity. For each value of $E_k$, the energy balance equation can be written based on the overall deformation of the SFRC beam:

$$E_k + E_{p,\ def.} = E_{max} \quad \rightarrow \quad 0.5mV_c^2 + (m+m')g\delta_{max} = \int_0^{\delta_{max}} f(\delta)d\delta; \quad E_k \leq E_{k,cr} \tag{12}$$

$$E_k + E_{p,\ def.} = E_{cap.} + E_k' \quad \rightarrow \quad 0.5mV_c^2 + (m+m')g\delta_u = \int_0^{\delta_u} f(\delta)d\delta + 0.5mV'^2; \quad E_k > E_{k,cr} \tag{13}$$

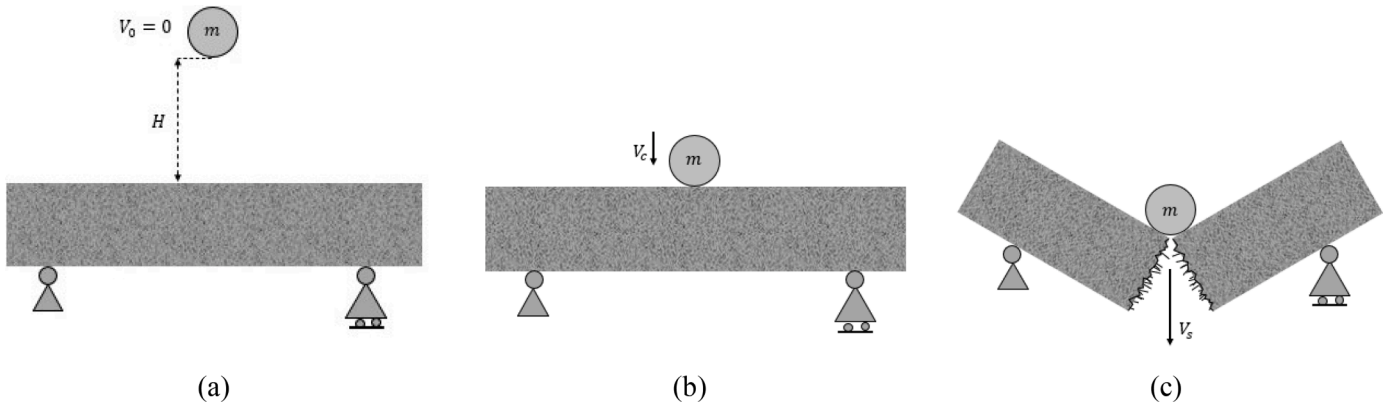


**Fig. 3.** Process of collision; (a) releasing the impactor; (b) contact moment; (c) after collision.

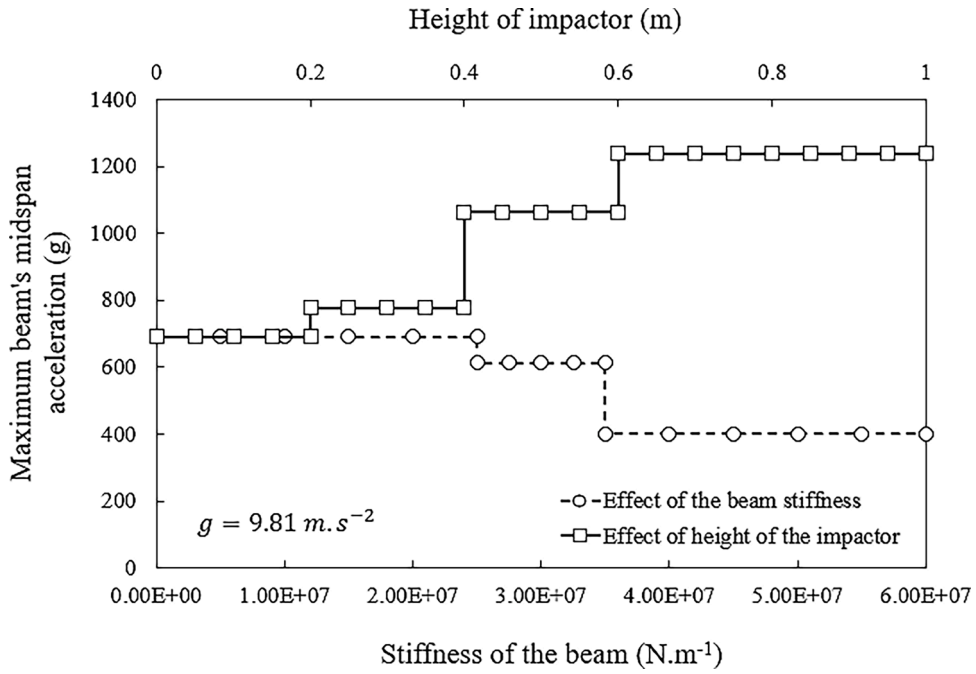


**Fig. 4.** Influence of $k$ and $H$ on the $\ddot{\delta}_{max}$ according to Eq. (7).

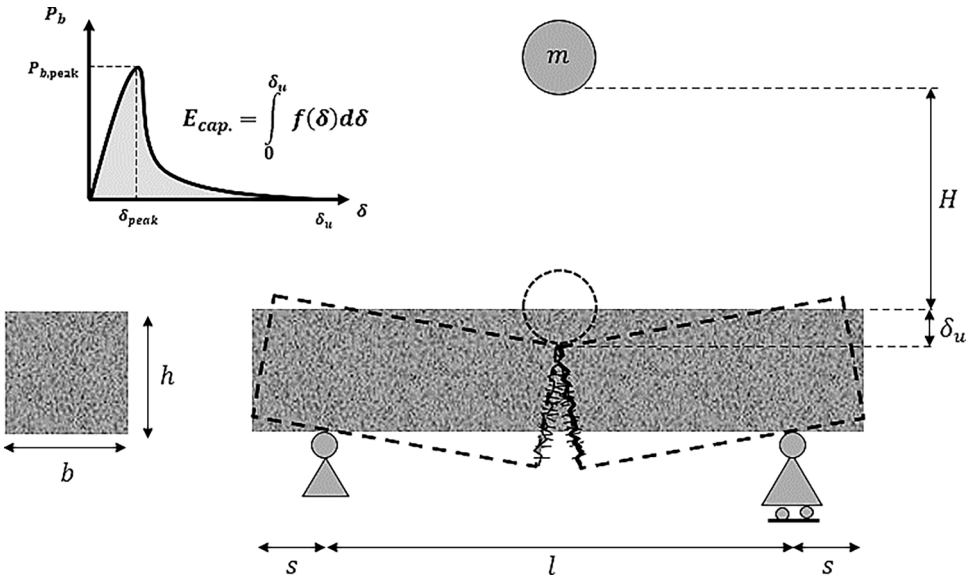


**Fig. 5.** Beam under impact load and entities used for the evaluation of the energy in impact loading.

$$V' = \left( V_c^2 + \frac{2(m+m')g\delta_u - 2\int_0^{\delta_u} f(\delta)d\delta}{m} \right)^{0.5} \quad (14)$$

where $E_{max}$ is the energy absorbed by the beam up to $\delta_{max}$ (maximum midspan deflection of the beam) in the first scenario, and $E_k'$ is the kinetic energy produced by the impactor at the moment of failure (when the beam attains $\delta_u$), and $V'$ is the velocity of the impactor at this moment, which can be determined from Eq. (14).

In the first scenario, the initial kinetic energy is lower than the critical one, condition provided by Eq. (12). In this case, the SFRC beam condition can be in both stages of the pre-peak in case of Eq. (15a) or to the post-peak (softening stage) in case of Eq. (15b). If the initial kinetic energy is higher than the critical one, second scenario condition provided by Eq. (13), the SFRC beam absorbed completely its fracture energy, a situation represented by Eq. (15a). In the options corresponding to Eqs. (15b) and (15c), the maximum total reaction force is attained, which is determined from the total reaction vs deflection relationship of the SFRC beam at $\delta = \delta_{peak}$. Since the impact force ($P_t$) is the sum of reaction forces ($P_b$) and inertia ($P_i$), and the inertia force is dependent on the contact velocity, the $P_t$ is different in the options corresponding to Eqs. (15b) and (15c). Based on the experimental results [9,11,13,15,30] obtained on the flexural behavior of SFRC beams under impact loading, a deflection softening stage generally occurs after peak point ($\delta_{peak}$, $P_{b,peak}$). Therefore, in this research, a softening behavior is assumed for post peak behavior of SFRC beams, Fig. 6.

$$P_b = f(\delta_{max}) \quad \rightarrow \quad P_t = f(\delta_{max}) + P_i, \quad E_k \le E_{k,cr} \text{ and } \delta_{max} < \delta_{peak} \tag{15a}$$

$$P_b = P_{b,peak} \quad \rightarrow \quad P_t = P_{b,peak} + P_i, \quad E_k \le E_{k,cr} \text{ and } \delta_{peak} \le \delta_{max} < \delta_u \tag{15b}$$

$$P_b = P_{b,peak} \quad \rightarrow \quad P_t = P_{b,peak} + P_i, \quad E_k > E_{k,cr} \tag{15c}$$

Furthermore, for achieving the time vs impact force diagram, the time interval of the impact load, $t_p$, must be obtained. Based on experimental results [11,13,23,28], Fig. 7 represents a typical time-force diagram. As shown in Fig. 7, the impact force-time diagram can be idealized by a positive and a negative force gradient up to $t_p$. The conservation of momentum can be expressed for the SFRC beam and impactor collision [27]. Due to the fact that the momentum of a system remains constant unless an outside force is applied [32], the impulse variation during impact loading, $\Delta P$, (area under the diagram of time vs total impact force) is equal to the difference between initial and stable momentum (when the impact force reaches a null value), $mV_c$ and $mV_s$, respectively, see Eqs. (16) and (17) and Fig. 3. The area under the idealized impact force-time diagram can be calculated based on the $P_t$ and $t_p$, ($\int_0^{t_p} f(t)dt = \frac{P_t \cdot t_p}{2}$).

$$\Delta P = mV_c - mV_s = \int_0^{t_p} f(t)dt \tag{16}$$

$$t_p = \frac{2m(V_c - V_s)}{P_t} \tag{17}$$

As soon as the impact force achieves a null value, the SFRC beam and the impactor displace at the same velocity, $V_s$. In this condition, according to the conservation of momentum, the momentum before collision is equal to the momentum of both the SFRC beam and the impactor with velocity of $V_s$. Therefore, the value of $V_s$ can be obtained from the following equation, which is in line with research performed by Zhao et al. [27]:

$$\Delta P = 0 \quad \rightarrow \quad (m + m')V_s = mV_c \tag{18a}$$

$$V_s = \frac{mV_c}{(m + m')} \tag{18b}$$

As it is challenging to ascertain the variations in displacement rate throughout the impact loading, a constant value is utilized to assess the loading rate effect on material characteristics. In this research, $V_s$ is considered as the maximum displacement rate under impact loading, $\dot{\delta}_d$.

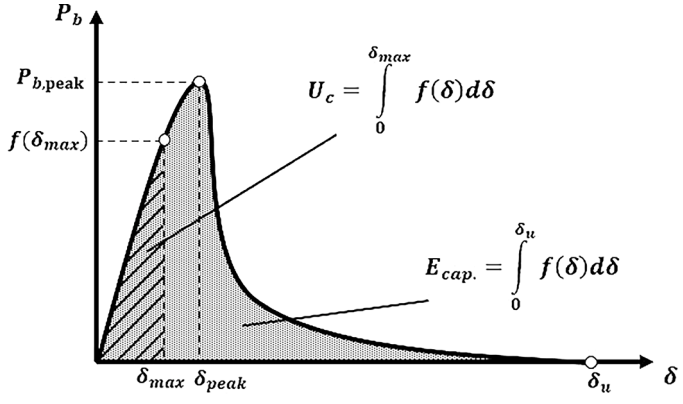


**Fig. 6.** Schematic representation of the total beam's reaction forces-deflection diagram of a SFRC beam.

### 2.3. Energy absorption capacity of SFRC beams (total beam's reaction forces-deflection diagram)

In this section, the total beam's reaction forces-deflection diagram is derived for a SFRC beam subjected to impact loading. For this purpose, firstly, the material properties of SFRC at compressive and tensile behavior under strain rate effects are defined. Then, the moment-curvature diagram for the cross-section of a beam is determined. Finally, using the unit-load method (see Appendix A), the total beam's reaction forces-deflection diagram is obtained.

#### 2.3.1. Constitutive laws

The stress-strain relation of SFRC materials have been investigated by numerous studies in the literature [33–39]. In the current study, the constitutive law proposed by Barros et al. [35] is utilized to simulate the uniaxial stress-strain relation of SFRC, since the effect of steel fiber content is considered as a direct parameter, Fig. 8a. The compressive stress-strain relation is expressed by Eqs (19):

$$\frac{\sigma_c}{f_{cm}} = \frac{\left(\frac{\varepsilon_c}{\varepsilon_{cl}}\right)}{(1 - p - q) + q\left(\frac{\varepsilon_c}{\varepsilon_{cl}}\right) + p\left(\frac{\varepsilon_c}{\varepsilon_{cl}}\right)^{(1-q)/p}} \tag{19a}$$

$$q = 1 - p - \frac{f_{cm}}{E_c \varepsilon_{cl}} \tag{19b}$$

$$\varepsilon_{cl} = 2.2 \times 10^{-3} + 0.0002 W_f \tag{19c}$$

where $f_{cm}$, $\varepsilon_{cl}$, $W_f$ and $E_c$ are the static compressive strength (MPa), the strain at peak stress, the fiber weight percentage in the mixture, and the initial tangent modulus of elasticity, respectively. The value of parameter $p$is between 0 and 1 and it is calculated by the Eq. (20):

$$p = 1 - 0.919 exp(-0.39 W_f) \tag{20}$$

It is assumed that the value of $E_c$ is the same for both tensile and compressive regimes and can be estimated by Eq. (21). It is considered that the ultimate compressive strain has a value of 0.0035. An additional assumption made is that any concrete layer whose compressive strain is greater than 0.0035 is deemed to have a null compressive strength capacity.

$$E_c = 2.15 \times 10^4 \left[\frac{f_{cm}}{10}\right]^{1/3} \tag{21}$$

The tensile behavior of the SFRC usually used in structural applications can be satisfactorily simulated by the three-linear stress-strain diagram represented in Fig. 8b, whose branches are reproduced by the Eqs (22) [35,40]:

$$\sigma_t = \begin{cases} E_c \varepsilon_t, & \varepsilon_t \le \varepsilon_{cr} \\ E_c \left(\frac{\alpha - 1}{p_1 - 1}\right)(\varepsilon_t - \varepsilon_{cr}) + f_{ctm}, & \varepsilon_{cr} < \varepsilon_t \le p_1 \varepsilon_{cr} \\ E_c \left(\frac{\alpha}{p_1 - p_2}\right)(\varepsilon_t - p_2 \varepsilon_{cr}), & p_1 \varepsilon_{cr} < \varepsilon_t \le p_2 \varepsilon_{cr} \end{cases} \tag{22a}$$

$$f_{ctm} = 1.4\left(\frac{f_{cm} - 8}{10}\right)^{2/3} \quad (f_{cm} \ in MPa) \tag{22b}$$

$$\alpha = 2s / l \tag{22c}$$

where $\varepsilon_{cr}$ is the strain at static tensile strength, $f_{ctm}$, $p_1$ and $p_2$ are multiples of $\varepsilon_{cr}$. The softening behavior is modelled by the mode I fracture parameters, namely, $f_{ctm}$, the fracture energy, $G_{Ff}$, and $\alpha$ and $p_1$ parameters defining the transition point between the two softening

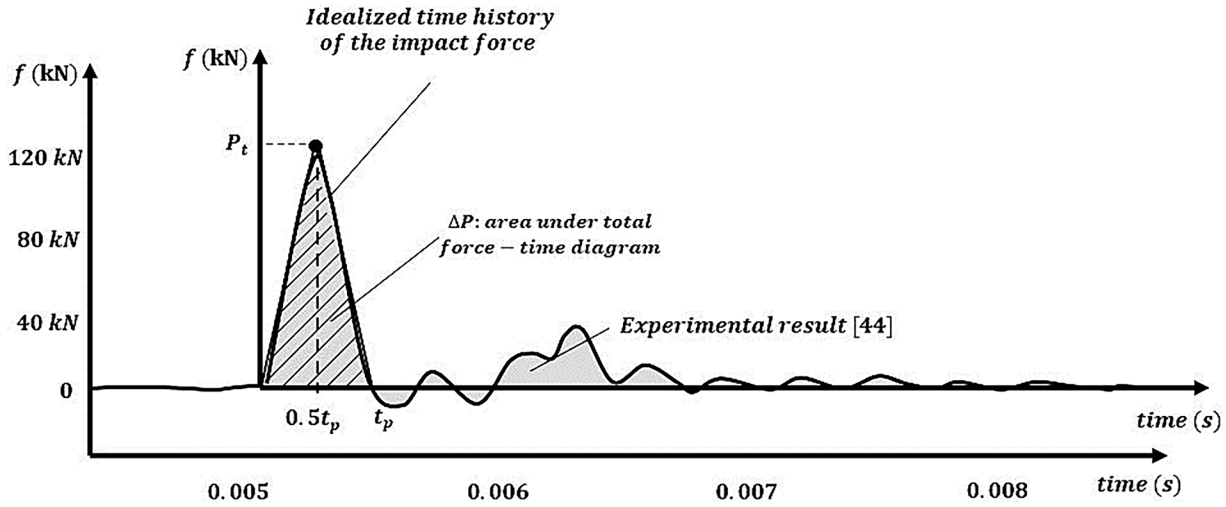


**Fig. 7.** Idealized time-force diagram.

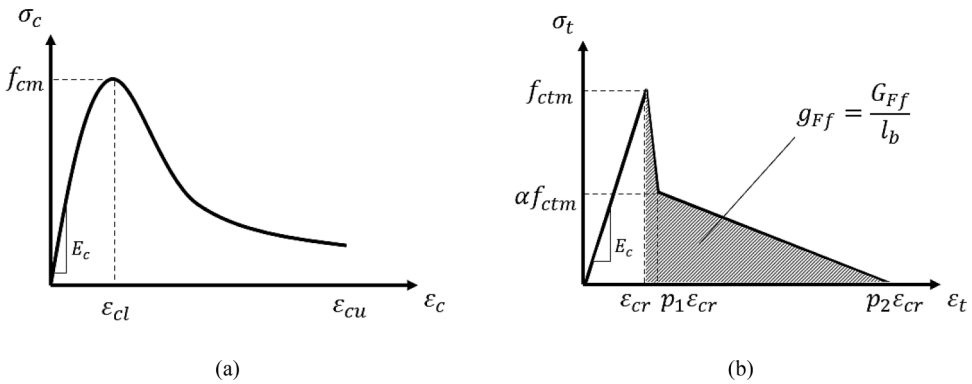


**Fig. 8.** (a) Compressive and (b) Tensile stress-strain relation for SFRC.

branches. Since strain concept is used for modeling the tensile softening stage, a characteristic length, $l_b = w/\varepsilon_t$, to bridge crack width with strain entities is used ($g_{Ff} = G_{Ff}/l_b$). According to Bazant and Oh [41], $l_b$ can be approximated as three times the maximum aggregate size. The $G_{Ff}$ of certain types of SFRC can be determined from Eq. (23a), where $G_F$ is the mode-I fracture energy of plain concrete of the same strength class of the SFRC, determined from Eq. (23d) [33]. The values defining the bilinear softening diagram ($p_1$ and $p_2$) can be derived from inverse analysis [42].

$$\frac{G_{Ff}}{G_F} = 19.953 + 3.213W_f \tag{23a}$$

$$l_b \simeq 3.\ D_{max} \tag{23b}$$

$$p_2 = \frac{2G_{Ff}}{\alpha l_b f_{ctm}\varepsilon_{cr}} - \frac{p_1 - \alpha}{\alpha} \tag{23c}$$

$$G_F = 73f_{cm}^{0.18} \qquad G_F[N/m] \ \ and \ \ f_{cm}[MPa] \tag{23d}$$

### 2.3.2. Strain rate effect

Since concrete is a material whose behavior depends on the strain rate that it is submitted to, constitutive laws must be also function of this variable. In this research, to determine the strain rate effect on the compressive behavior of SFRC, both modulus of elasticity and compressive strength are calculated according to *fib*-Model Code 2010 recommendations, Eqs. (24) and (25), [33]. Due to fiber-bridging action, fiber reinforcement affects more predominantly the concrete tensile behavior rather than its compressive behavior. Hence, the model proposed by Malver and Ross [39] is adopted for considering the effect of strain rate on the tensile strength of SFRC, since it has demonstrated good predictive performance regarding the experimental results, Eq. (26a).

$$\frac{f_{cm,dy}}{f_{cm}} = \begin{cases} \left(\dfrac{\dot{\varepsilon}_c}{30\times10^{-6}}\right)^{0.014}, & \dot{\varepsilon}_c \le 30\ s^{-1} \\ 0.012\left(\dfrac{\dot{\varepsilon}_c}{30\times10^{-6}}\right)^{1/3}, & \dot{\varepsilon}_c > 30\ s^{-1} \end{cases} \tag{24}$$

$$\frac{E_{c,dy}}{E_c} = \left(\frac{\dot{\varepsilon}_c}{30\times10^{-6}}\right)^{0.026} \tag{25}$$

$$\frac{f_{ctm,dy}}{f_{ctm}} == \begin{cases} \left(\dfrac{\dot{\varepsilon}_t}{1\times10^{-6}}\right)^{\mu}, & \dot{\varepsilon}_t \le 1\ s^{-1} \\ \beta\left(\dfrac{\dot{\varepsilon}_t}{1\times10^{-6}}\right)^{1/3}, & \dot{\varepsilon}_t > 1\ s^{-1} \end{cases} \tag{26a}$$

$$\mu = (1 + 0.6f_{cm})^{-1} \tag{26b}$$

$$log(\beta) = 6\mu - 2 \tag{26c}$$

where $E_{c,dy}$ and $f_{cm,dy}$ represent the modulus of elasticity and the compressive strength of SFRC under compressive strain rate ($\dot{\varepsilon}_c$), and $f_{ctm,dy}$ is the tensile strength of SFRC under tensile strain rate ($\dot{\varepsilon}_t$). Due to the fact that the compressive strength of concrete is typically much greater than its tensile strength, the behavior of an SFRC beam (without

longitudinal reinforcement) is frequently controlled by its tensile behavior. As a result, the tensile modulus of elasticity, tensile strength, and fracture energy of the SFRC are crucial parameters for determining the beam behavior under impact load. Using the modulus of elasticity obtained from compressive testing, a linear stress-strain relationship was utilized to model the pre-cracking tensile behavior. The fracture energy of SFRC is approximately estimated by Eq. (23a) and the effect of loading rate is simulated by Eq. (27). The model proposed by Zhang et al. [23] is utilized for defining the DIF of fracture energy to investigate the strain rate effect on the fracture energy of SFRC, as follows:

$$DIF_G = \frac{G_{Ff,dy}}{G_{Ff}} = 1 + \left(7.6 \times 10^{-6}\right)\left(\frac{\dot{\delta}_d}{1mm/s}\right)^{1.54} \tag{27}$$

where $G_{Ff}$ and $G_{F,dy}$ are the SFRC fracture energy under static (calculated by Eq. (23a)) and dynamic flexural loading conditions, respectively, while $\dot{\delta}_d$ is the dynamic midspan displacement rate. Based on the beam bending theory for the three-point bending test in linear phase before cracking, the relationship between the midspan deflection rate, $\dot{\delta}_d$, and the strain rate, $\dot{\varepsilon}_c = \dot{\varepsilon}_t$, at the extreme surfaces of the cross section can be obtained from the following equation [28]:

$$\dot{\varepsilon}_c = \dot{\varepsilon}_t = \frac{6h\dot{\delta}_d}{l^2}, \qquad \dot{\delta}_d = V_s \tag{28}$$

According to the experimental results [14–17,23] and for sake of simplicity, under impact load, the post peak tensile behavior of SFRC can be assumed linear with respect to the strain rate effect on the fracture energy under these circumstances, Fig. 9b. The strain rate has an equal effect on both the fracture energy and fracture energy density, $g_{Ff}$ (defined as the area under the stress-cracking strain diagram), assuming that $l_b$ under dynamic and static loading is the same.

$$DIF_G = \frac{G_{Ff,dy}}{G_{Ff}} = \frac{g_{Ff,dy}}{g_{Ff}} \tag{29}$$

where $g_{Ff} = G_{Ff}/l_b$ and $g_{Ff,dy} = G_{Ff,dy}/l_b$ are respectively the area under the static and dynamic post-cracking tensile stress-strain diagram, Fig. 9.

To determine the tensile and compressive behavior of SFRC under impact load, it is important to consider that the fracture mechanism of this composite material varies with the loading rate, [43]. It is hypothesized that cracks in the matrix parts of SFRC start in the weaker interfacial transition zone (ITZ) between the aggregate and the matrix. These cracks then propagate through the matrix until they connect with other ITZs, eventually resulting in a complete rupture of the specimen. In another word, during quasi-static loading, propagating cracks have adequate time to find the path of least resistance. However, under higher loading rates, cracks form rapidly and are compelled to propagate through the shortest available path, which may comprise elements with higher resistance, such as aggregates, leading to an increase in strength.

On the other hand, based on the experimental study performed by Ulzurrun et al. [11], it was observed that by increasing the loading rate (height of impactor), the susceptibility of fiber rupture increases. This can be justified by the increase of the friction coefficient with the slip rate in the fiber pullout mechanism [44] and the higher stiffness response of the surrounding concrete matrix when submitted to higher pressure rate of due to fiber pullout, mainly by inclined fibers toward the crack plane, [45]. The fiber reinforcement performance depends on the strain rate, the geometry and the tensile strength of the fiber, [11]. In the range of quasi-static displacement rate, smooth fibers exhibit a clear dependency on displacement pullout rate, whereas hooked-end fibers can be considered largely insensitive to it, [43,44]. Under impact loading, hooked-end fibers are more prone to rupture when the strain rate is increased, [15]. In the case of concrete reinforced with smooth fibers, the mandatory fiber failure mechanism is pullout (debonding), regardless of the loading rate, [15].

By increasing the strain rate loading conditions of concrete reinforced with steel fibers (considering the different failure mechanisms of pull-out, debonding, and rupture), the load carrying capacity and pre-peak stiffness of this composite increase, but its ductility decreases, which is reflected in the bilinear stress-strain relationship proposed in Fig. 9b, [15]. The pre-peak phase is approximated by a linear branch whose stiffness is simulated by the dynamic modulus of elasticity, $E_{c,dy}$, estimated by Eq. (25). By considering $\varepsilon_{cr,dy} = f_{ct,dy}/E_{c,dy}$, assuming the characteristic length not dependent on the strain rate and determining the dynamic tensile strength, $f_{ct,dy}$, and fracture energy, $G_{Ff,dy}$, from Eqs. (26a) and (27), respectively, the softening branch is directly characterized. For this purpose, the coefficient $\xi$ is proposed in the present study:

$$\xi = \frac{2E_{c,dy}G_{Ff,dy}}{l_b f_{ctm,dy}^2} + 1 \tag{30}$$

$\varepsilon_{cr}$ and $\varepsilon_{cr,dy}$ are the strain correspond to peak tensile strength in static and dynamic loading conditions, respectively, while $\xi$ is a multiple of the $\varepsilon_{cr,dy}$, defining the ultimate tensile strain under dynamic loading conditions.

### 2.3.3. Moment-curvature diagram

The beams force-deflection response can be predicted with the moment-curvature relationship ($M-\chi$) determined from a layered-section approach that considers the constitutive laws of the materials used, strain compatibility (assuming linear strain distribution along the section for both quasi-static and dynamic behavior) and force equilibrium, Fig. 10a. In the current study, the sectional analysis software

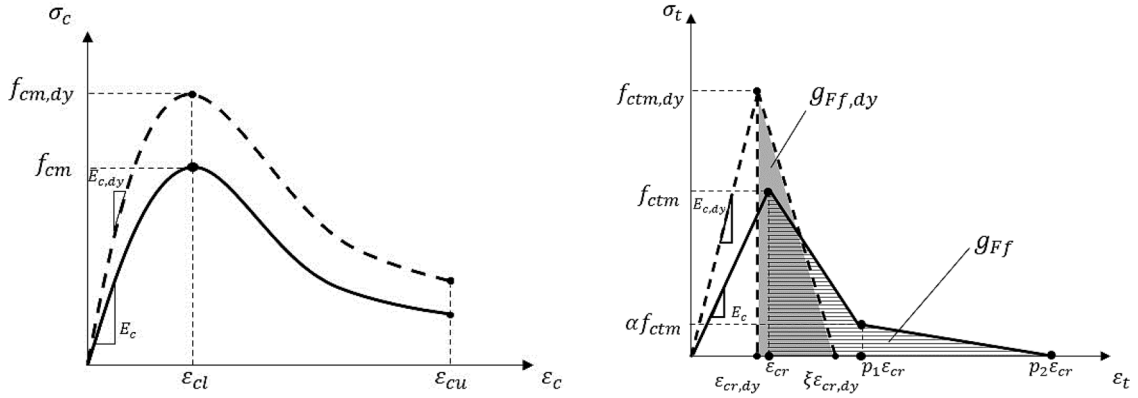


**Fig. 9.** Proposed method for defining the dynamic (a) compressive and (b) tensile behavior of the SFRC.

DOCROS [46] is used to determine the $M-\chi$ relationship of a cross-section, Fig. 10b. Both tensile and compressive stress-strain relations of SFRC are modified for dynamic loading according to the suggestions presented in previous section and were used as a material properties model in DOCROS.

### 2.3.4. Beam's reaction forces-deflection diagram

To derive the total reaction force-deflection diagram of a SFRC beam subjected to impact loading, the bending moment, $M(x)$, and shear force, $V(x)$, diagrams must be calculated by considering the effect of inertia force, Fig. 11. Considering the beam's geometry and total inertia force to total applied force ratio, $\psi$, the shear force and bending moment diagrams are calculated from the Eqs. (5a) and (5b). The total inertia force, $P_i$, is calculated by Eq. (2) and $\psi$ is a function of $P_b$, Eq. (6).

The span-depth ratio of short beam specimens normally used for laboratory testing frequently lies in the range of 2 – 4 and, therefore, shear can have a non-negligible contribution for the total deflection of the beam. Consequently, the beam's total deflection, $\delta$, considers the addition of the parcel due to bending, $\delta_m$, with the parcel due to shear, $\delta_v$. The unit-load method (or conjugate-beam) is used to obtain the total deflection [47], according to Eq. (31),

$$\delta = \delta_m + \delta_v = \int_0^l \frac{M_{un}.M_l}{EI}dx + \int_0^l \frac{V_{un}.V_l}{GA.f_{sh}}dx \tag{31}$$

where $M_{un}$ and $M_l$ are the bending moment diagrams due to a unit load configuration (corresponding to the deflection to be obtained) and the real load configuration the beam is subjected, respectively; $EI$ is the flexural stiffness of the beam's cross section; $V_{un}$ and $V_l$ are the shear force diagrams due to the unit load configuration and the real load configuration, respectively; $GA.f_{sh}$ is the shear stiffness of the beam's cross section [47], where $f_{sh}$ is the shear shape factor that for rectangular cross sections is equal to 5/6. In a nonlinear analysis, $EI$ and $GA.f_{sh}$ should decrease with the damage induced in the cross sections due to the applied bending moments and shear forces. $\delta_m$ can be calculated by using the conjugate-beam method and replacing $M_l/EI$ in Eq. (31) by the corresponding curvature, $\chi$. For each value of bending moment along the beam, Eq. (5a), the $\chi$ value is obtained from the $M-\chi$ relationship derived from the sectional analysis by software DOCROS [46]. The $M-\chi$ diagram of the beam can be divided in two parts, namely, pre-peak and post-peak, see Fig. 11.

In pre-peak part (up to the peak moment, $M_{peak}$), all beam length is in the pre-peak stage and the curvature distribution along the beam is obtained from the moment-curvature diagram shown in Fig. 11a. In another word, by applying the amount of $\chi$ as a distributed load along the conjugate-beam, the bending moment at each point of the conjugate-beam length would be equivalent to its deflection along the original-beam (see A. Calculating of beam's total reaction force-deflection diagram).

In post-peak part, for a major part of SFRC used in real applications, the $M-\chi$ response of a representative cross section presents a softening stage for curvatures higher than the curvature corresponding to the peak moment, $\chi > \chi_{peak}$. It means that although the curvature continues to increase, the bending moment decreases. In this case, the conjugate-beam method must be modified for this condition to consider the softening behavior of SFRC beam in the post-peak stage. At this stage ($\chi > \chi_{peak}$), it is assumed that the beam's midspan (point B of the beam in Fig. 11) is only transfer to the post-peak stage and follows the softening portion of the $M-\chi$ relationship which is in the line of Elsaigh et al. [48] findings, Fig. 12. It means that a pseudo-plastic hinge occurs at midspan of the beam with a negligible length that can be considered as a point, (point B of the beam in Fig. 13). While the other sections of the beam enter in an unloading stage with slope of $(EI)_{sec} = M_{peak}/\chi_{peak}$ (Fig. 12). Therefore, the force applied to the beam decreases while the crack width and deflection at the midspan increases. For calculating the midspan deflection, in addition to the distributed curvature due to distributed moment along the beam, the post-peak increment of curvature $[(\chi_s - \chi_{peak}).2\Delta x]$ is applied to the beam's midspan as a point load, Fig. 13. The point curvature at the midspan $[(\chi_s - \chi_{peak}).2\Delta x]$ explains the effect of increasing crack width at the beams midspan, see A. Calculating of beam's total reaction force-deflection diagram. For simplifying the calculation process, the beam's length is divided in small segments of length $\Delta x$, see Fig. 12. It should be noted that this method has been also used for predicting the load-deflection in four-point bending tests, [48].

The deflection due to the contribution of shear deformation, $\delta_v$, can be calculated by using the conjugate-beam method and replacing $V_l/GAf_{sh}$ in Eq. (31) with the corresponding shear strain, $\gamma$. For each value of shear force along the beam, Eq. (5a), the $\gamma$ can be obtained from the linear part of the $V-\gamma$ relationship which is in line with the research of Elsaigh et al. [48] and Bryan et al. [49], see Fig. 14a. At any stage throughout the loading process, shear strains on the $V-\gamma$ response shown in Fig. 14a are calculated by dividing the shear force to the shearing stiffness which is assumed constant for SFRC beam. The shear force can be obtained from the shear diagram of the beam. Referring to the load configurations shown in Fig. 14b, the shear deflection in the beam is due to the shear forces in parts AB and BC. At the onset of the flexural cracks at midspan, these two parts unload elastically which result in less complexities compared to that followed for the moment-curvature analysis.

In other words, by applying the amount of $\gamma$ as a distributed load along the conjugate-beam, the shear force at each point of the conjugate-beam length would be equivalent to its deflection along the original-beam, see A. Calculating of beam's total reaction force-deflection diagram. By increasing the total force at the beam's midspan up to the peak

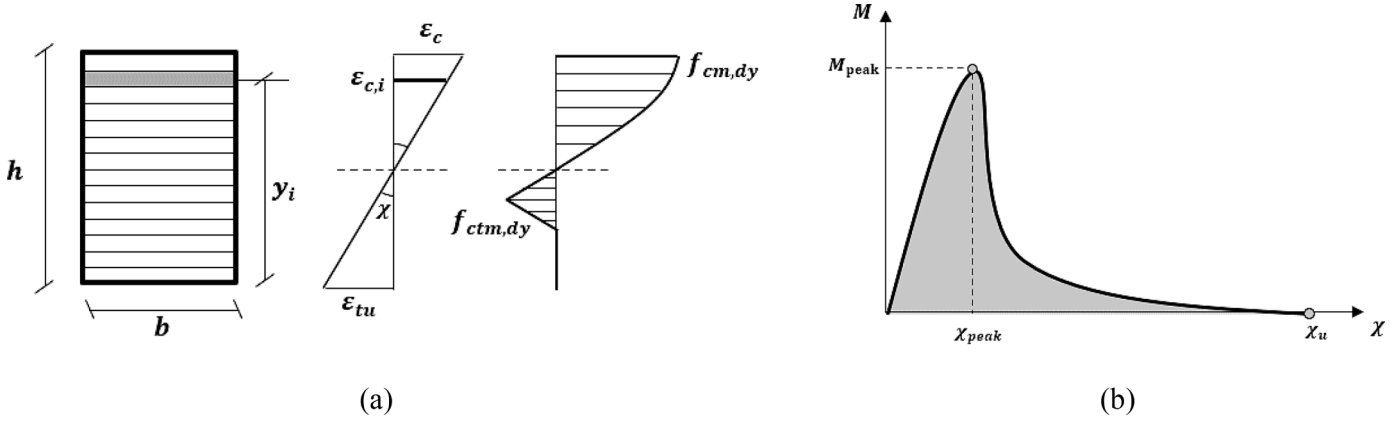


**Fig. 10.** (a) Layered approach with compatibility of strains and stress diagram; (b) Moment-curvature relationship for a SFRC section from a section analysis.

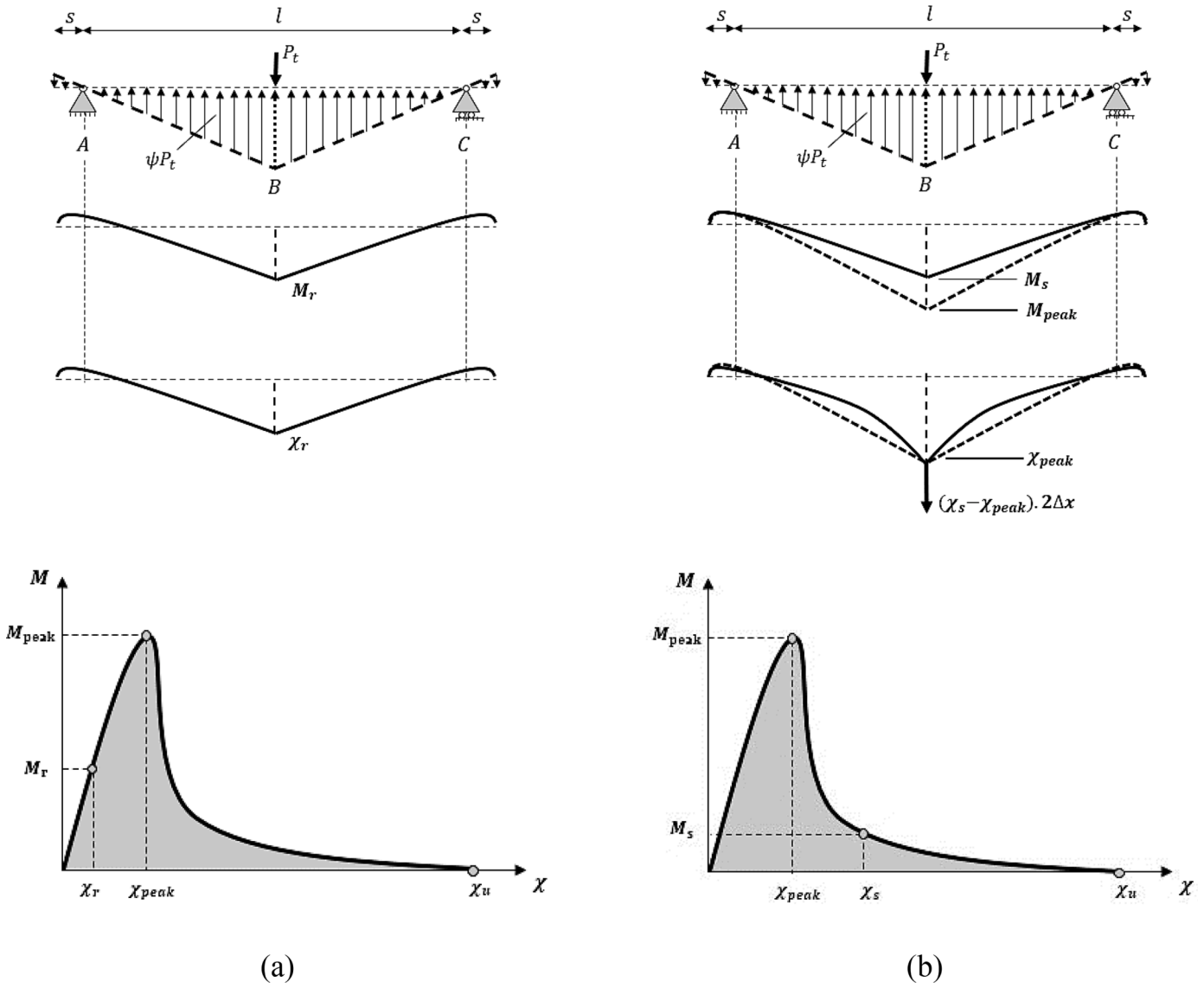


**Fig. 11.** Moment and curvature distributions and moment-curvature relationship for an applied load, $P_t$, at (a) pre-peak stage; (b) post-peak stage.

shear force, $V_{peak}$, the midspan deflection, shear force and shear strain increase. As soon as the shear force reaches $V_{peak}$ (when the moment reaches to $M_{peak}$), although the midspan deflection increases, the shear force and shear strain decrease and the effect of shear strain on the midspan deflection is reduced. Fig. 15 shows the free-body diagram for the conjugate-beam for calculating $\delta_v$.

Finally, the total deflection was calculated by using the superposition concept as the sum of both effects ($\delta_v$ and $\delta_m$). Considering both effects of shear force and bending moment on the deflection at the beam's midspan, the impact force-deflection relation is obtained for simply supported SFRC beam. The flowchart of the model is represented in Fig. 16.

As shown in Fig. 16, at first, the input data considered is beam geometry, concrete density, fiber volume percentage, compressive strength of the matrix, impactor mass and height. According to the input data, the quasi-static behavior of SFRC is obtained. In the next step, according to the loading rate resulting from the contact velocity of the impactor and concrete, the dynamic behavior of SFRC is obtained. Next, the force-displacement diagram on the midspan of the beam can be drawn by considering the inertial force along the beam. The initial kinetic energy applied by the impactor is determined and compared with the critical kinetic energy of the beam. Then, according to the energy dissipation capacity of SFRC beam, the maximum force [$f_{peak}$ (post-peak stage) or $f(\delta_{max})$ (pre-peak stage)] is calculated. Finally, according to the obtained maximum force, the impact and the beam reaction forces are determined.

## 3. Assessment of the proposed model

### 3.1. Experimental database

A database consisting of 121 SFRC beams that were tested under drop-weight impact at midspan was gathered from previous studies in this field, [9–15,23,47] to validate the proposed model for predicting the peak response of SFRC beams under impact loading. All considered specimens in the present study were simply supported SFRC beams with rectangular cross-section tested under impact loading by the impactors with a spherical shape nose. In order to gain a better understanding of the data collected, the range and frequency percentage of some of the basic parameters in the models are given in Fig. 17 and Table 3.

### 3.2. Sensitivity analysis

A sensitivity analysis was performed for the reaction force-deflection diagram considering some parameters such as compressive strength,

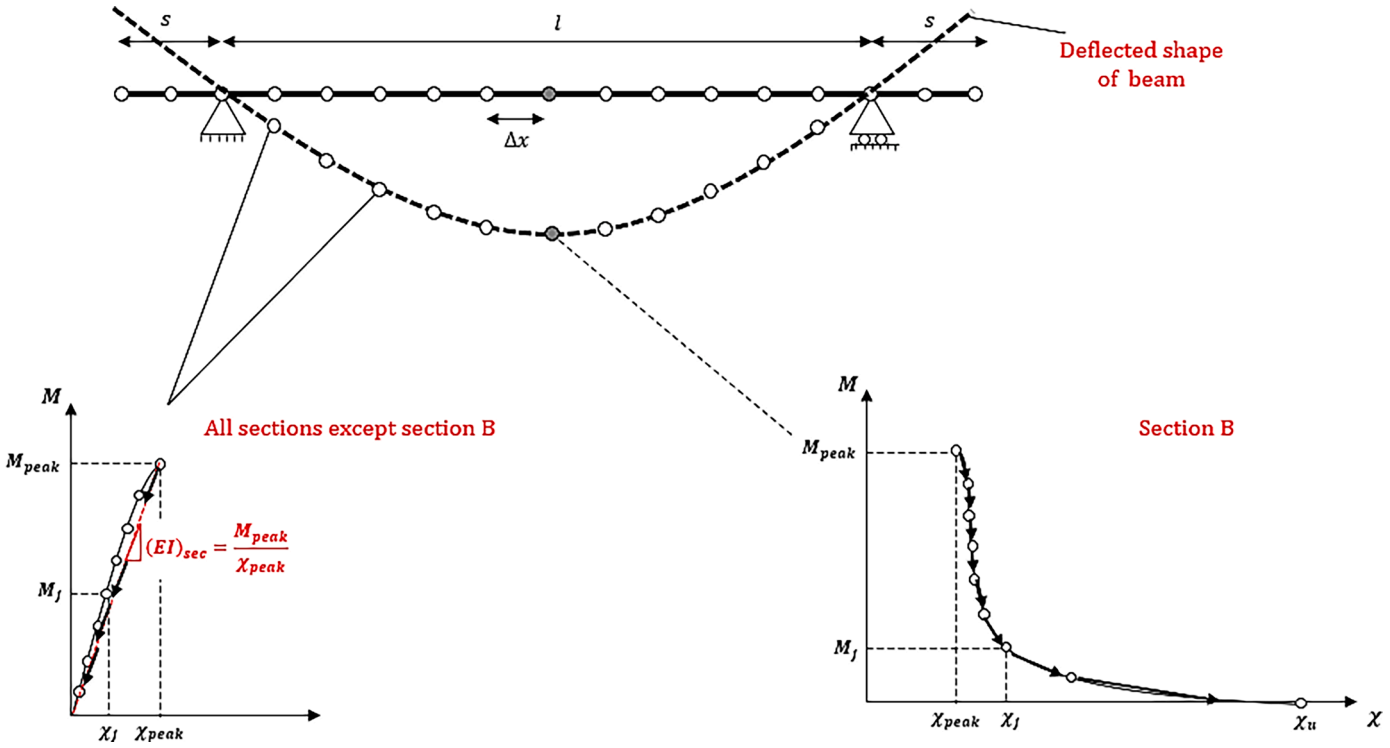


**Fig. 12.** Free-body diagram for the conjugate-beam at (a) pre-peak stage; (b) post-peak stage.

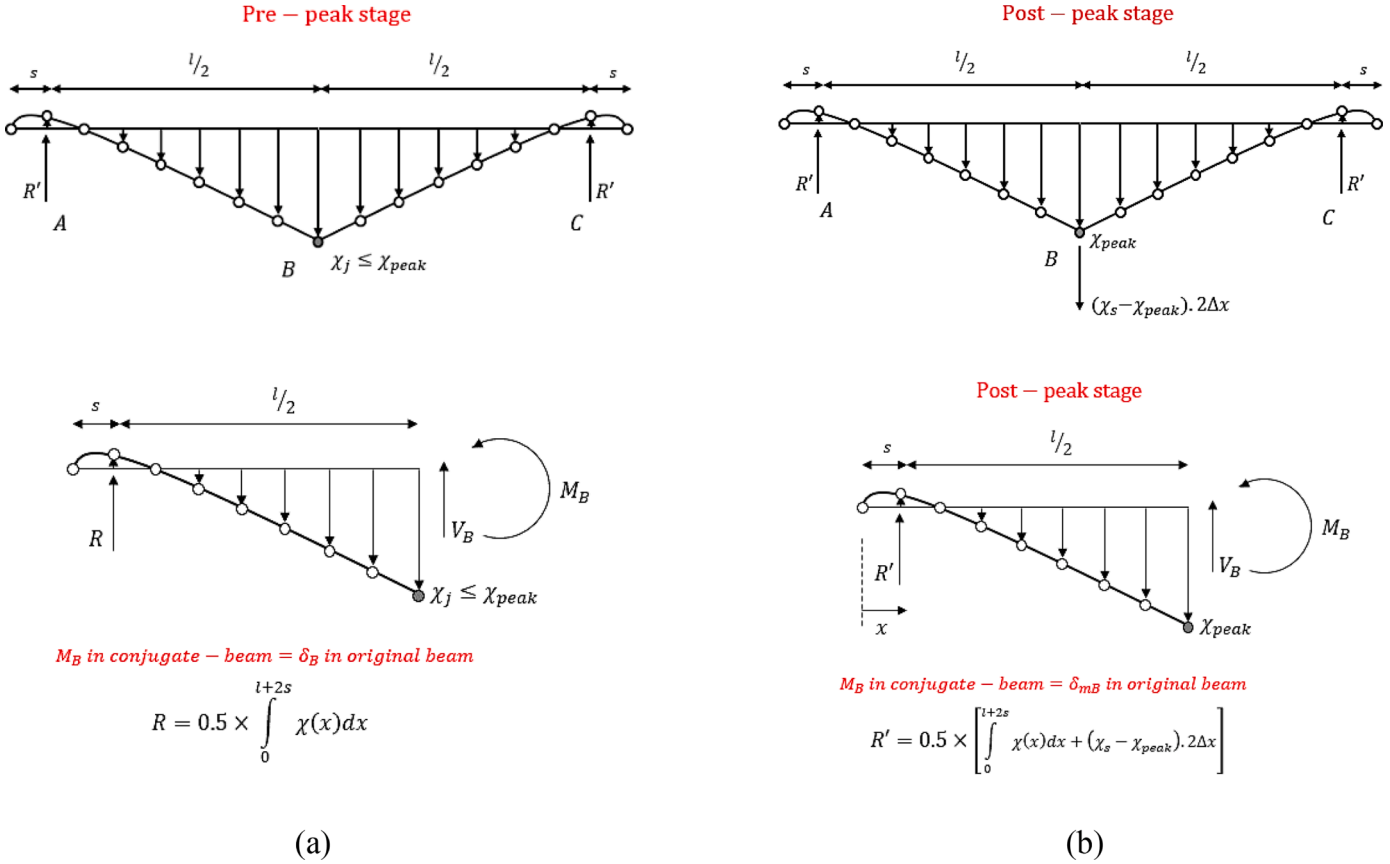


**Fig. 13.** Free-body diagram of the conjugate-beam for calculating $\delta_m$ at (a) pre-peak stage; (b) post-peak stage.

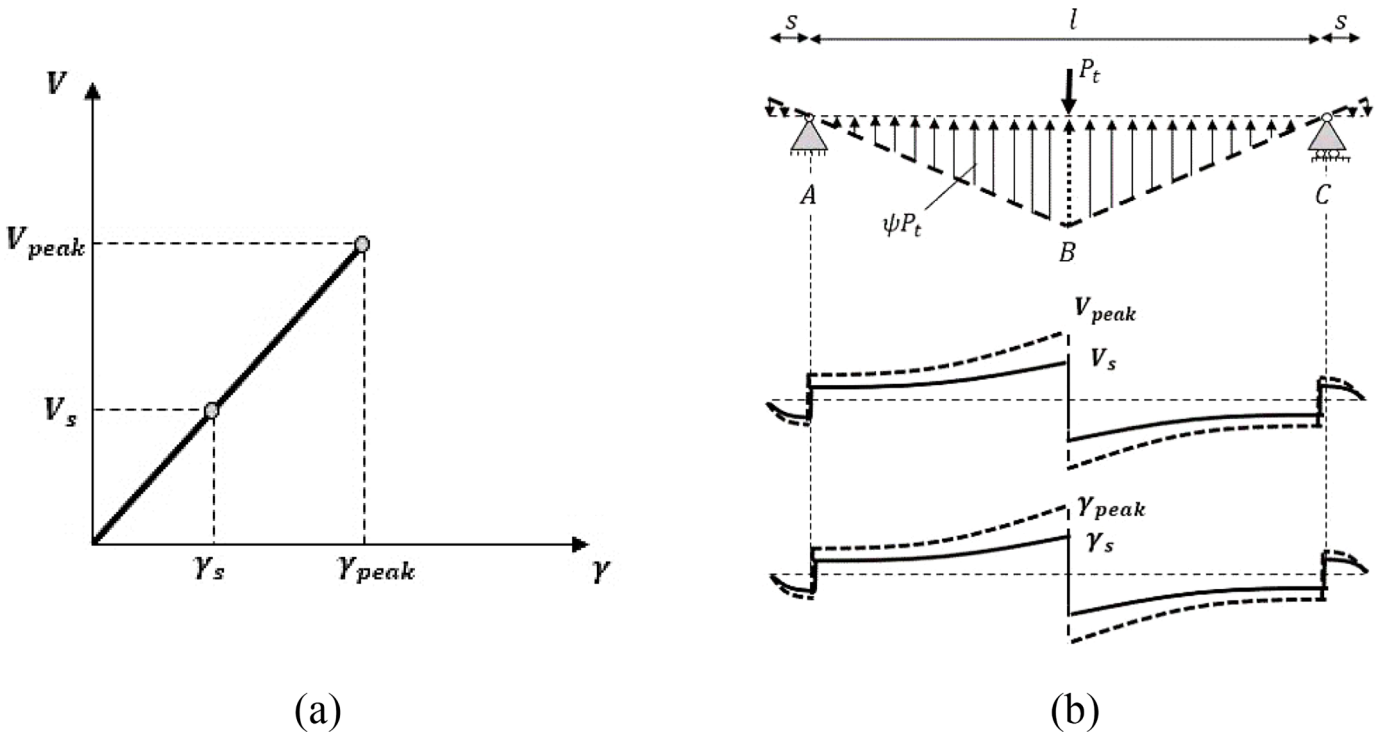


**Fig. 14.** (a) Shear force - shear strain relationship; (b) shear force and shear strain distributions for an applied load.

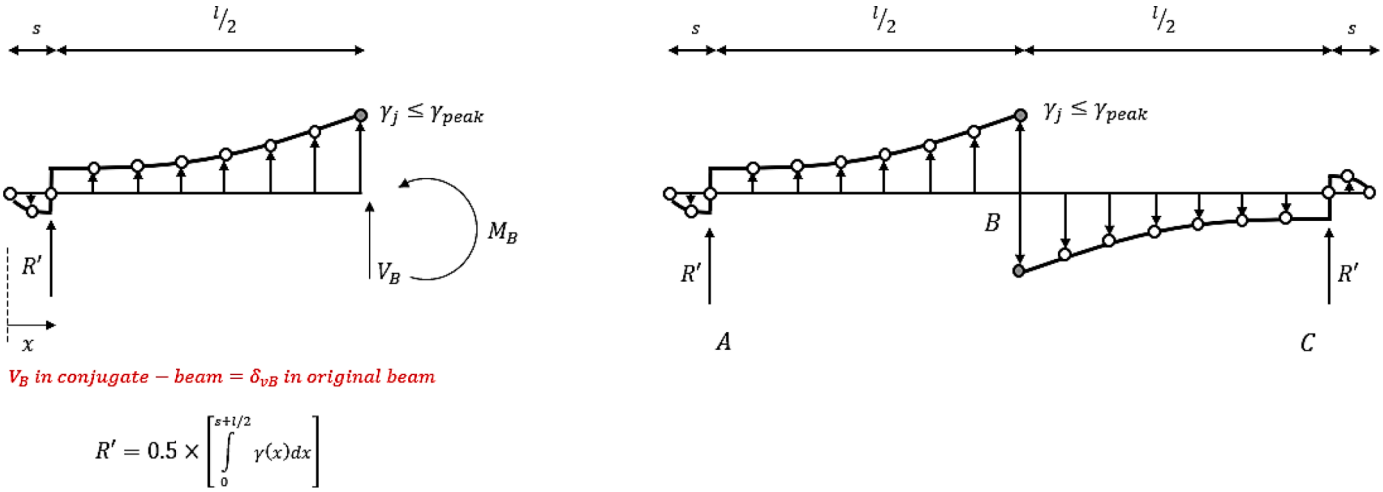


**Fig. 15.** Free-body diagram for the conjugate-beam for calculating $\delta_v$.

fiber weight percentage, impactor velocity, and beam's span length to height ratio. The relevant results are represented in Fig. 18. The experimental result of the reaction force-deflection behavior conducted by Zhang et al. [23] was used to analyze the sensitivity of the model to the important parameters, Table 4. The different values of compressive strength used for evaluation were 40, 80, 120, 160, and 200 MPa. An increase of 245% occurred in the reaction force capacity when this parameter increased from 40 to 200 MPa. Similarly, different values were selected for fiber weight percentage. The reaction force increases with the fiber weight percentage due to a positive effect on the post-peak behavior of SFRC. In addition, the effect of using different impactor velocities (contact velocity) on the reaction-force-deflection behavior of the SFRC beam was represented in Fig. 18. The sensitivity analysis due to the geometry of the SFRC beam was observed by studying the span length to height ratios of 2, 3, 4, 5, and 6, respectively. Increasing the beam's span length to height ratio decreases the reaction force while causing an increase in the peak and ultimate deflections.

### 3.3. Peak impact force validation

To validate the peak impact force predicted by the proposed model, some experimental results in literature [11,15,23]) were considered and the total SFRC beam's reaction forces-deflection responses under impact loading presented in the literature and obtained from the proposed model were compared as a design example. B. Example from literature (Zhang et al. [23]) for obtaining impact response of show the calculation of reaction-force deflection and impact-time diagrams of the SFRC beam in detail. The input data of three specimens tested under drop weight impact are shown in Table 4.

From Eqs. (1) to (14), the energy balance relationships can be written for the present SFRC beam, and based on the obtained reaction force-deflection diagram, the peak impact forces and maximum reaction

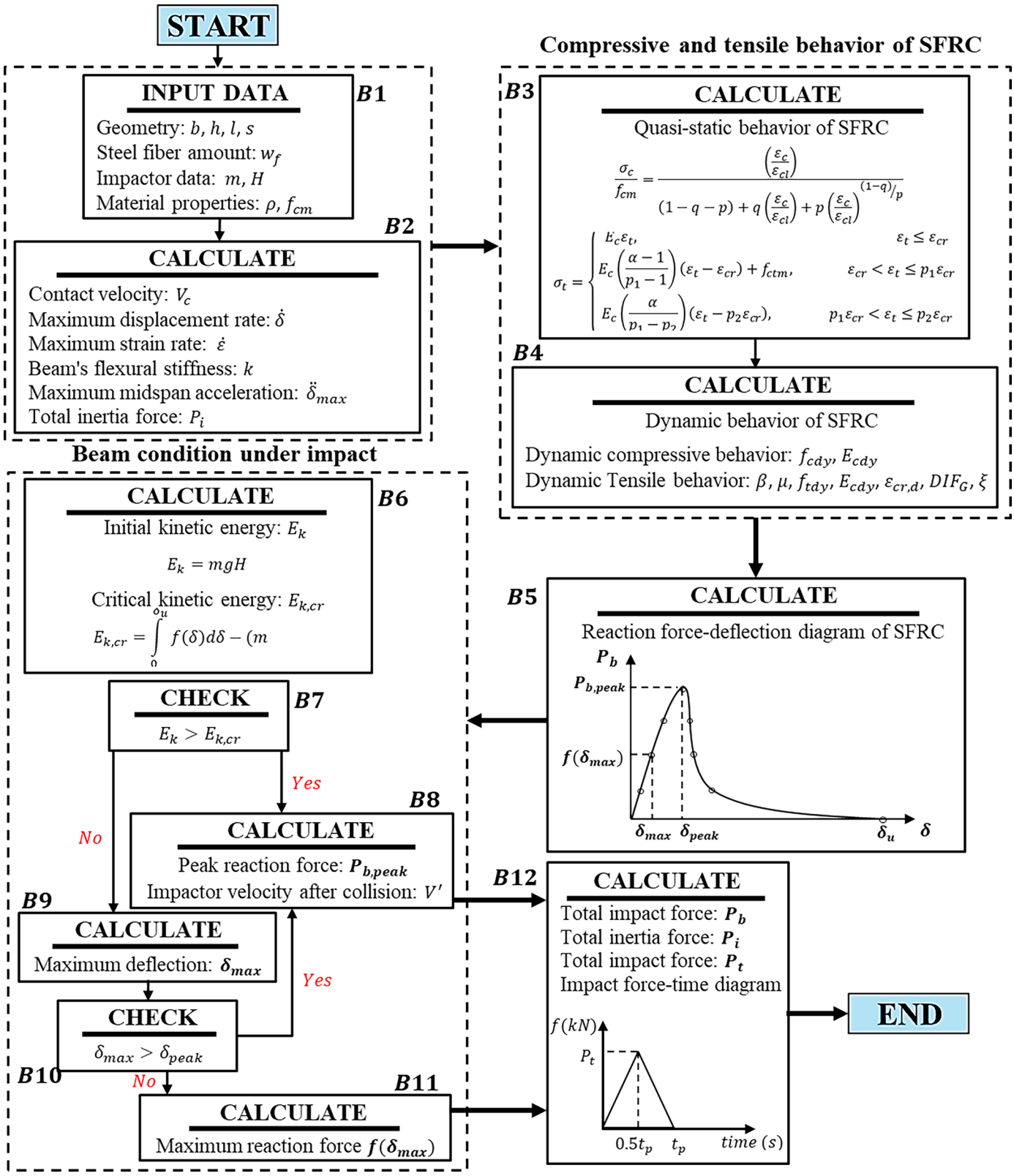


**Fig. 16.** Flowchart to determine the peak impact force using energy-balance model.

forces are calculated using Eq. (15a). Fig. 19 shows the correlations between calculated and experimental [11,15,23] total beam's reaction forces-deflection responses and impact-time diagram during impact process. The model error in estimating the peak impact force for the beams #1, #2, and #3 is 0.7, 17.8, and 10.6%, respectively, which means that the analytical method can calculate the experimental result with satisfactory accuracy.

This method was applied to predict all obtained results from the literature review. According to the calculated results and their comparison with experimental results, the approach used is deemed to be

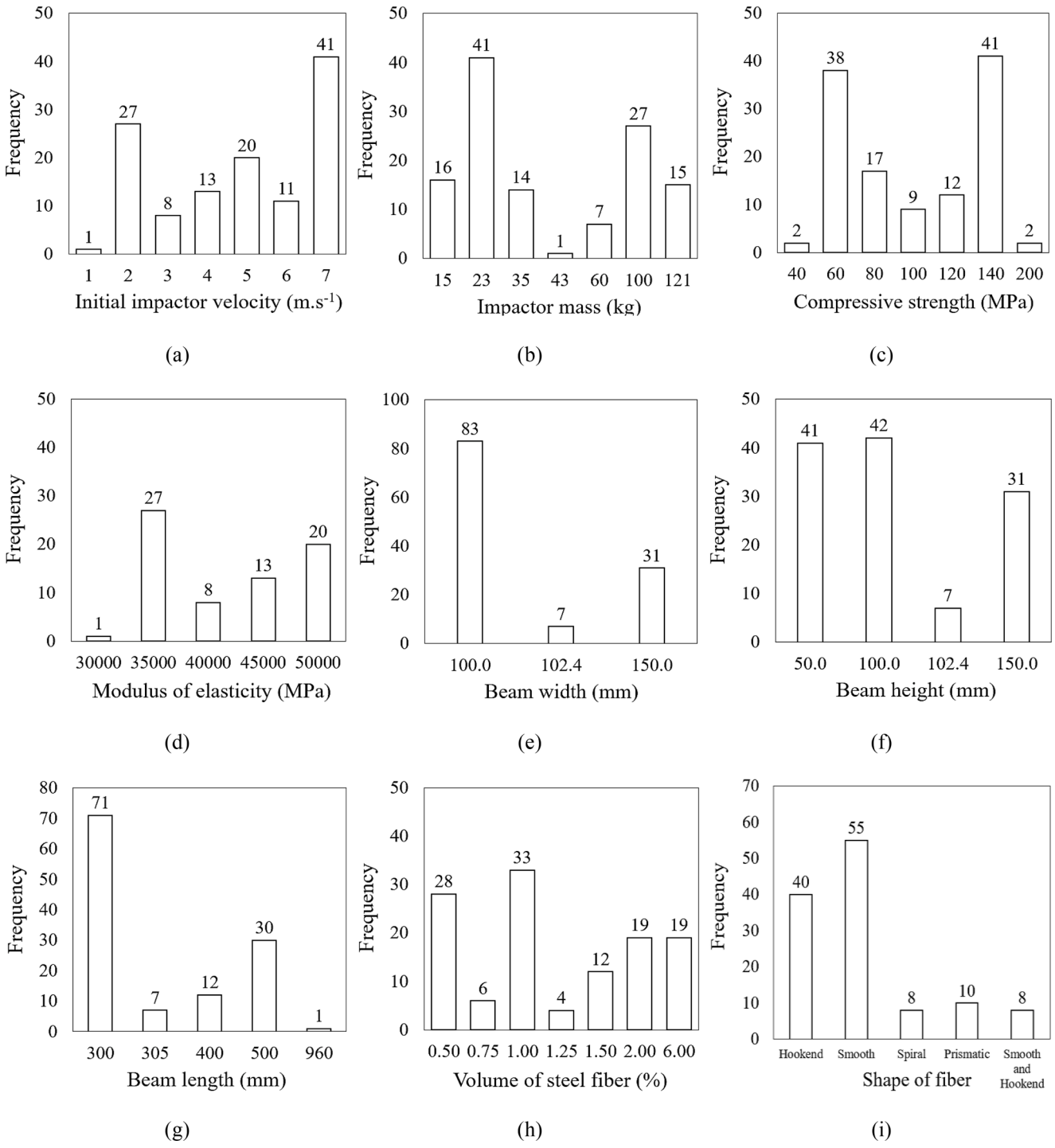


**Fig. 17.** Distribution of the experimental parameters; (a) impactor velocity; (b) impactor mass; (c) SFRC compressive strength; (d) SFRC modulus of elasticity; (e) beam width; (f) beam height; (g) beam length; (h) steel fiber volume; (i) shape of fiber.

**Table 3**
Range and most frequent of each experimental parameter.

| Parameter | Min. | Max. | Most frequent | Parameter | Min. | Max. | Most frequent |
|---|---|---|---|---|---|---|---|
| Impactor velocity [m.$s^{-1}$] | 0.89 | 6.26 | 6.26 | Impactor mass [kg] | 15 | 120 | 23 |
| Compressive strength [MPa] | 34 | 229 | 140 | Modulus of elasticity [GPa] | 29 | 49 | 35 |
| Initial kinetic energy [J] | 35 | 1716 | 500 | Beam span length [mm] | 300 | 960 | 300 |
| Beam length [mm] | 350 | 980 | 350 | Beam height [mm] | 50 | 150 | 100 |
| Beam width [mm] | 100 | 150 | 100 | SF volume [%] | 0.00 | 6.00 | 1.00 |
| SF shape | – | – | Smooth | SF aspect ratio | 50 | 101 | 65 |

SF: Steel Fiber

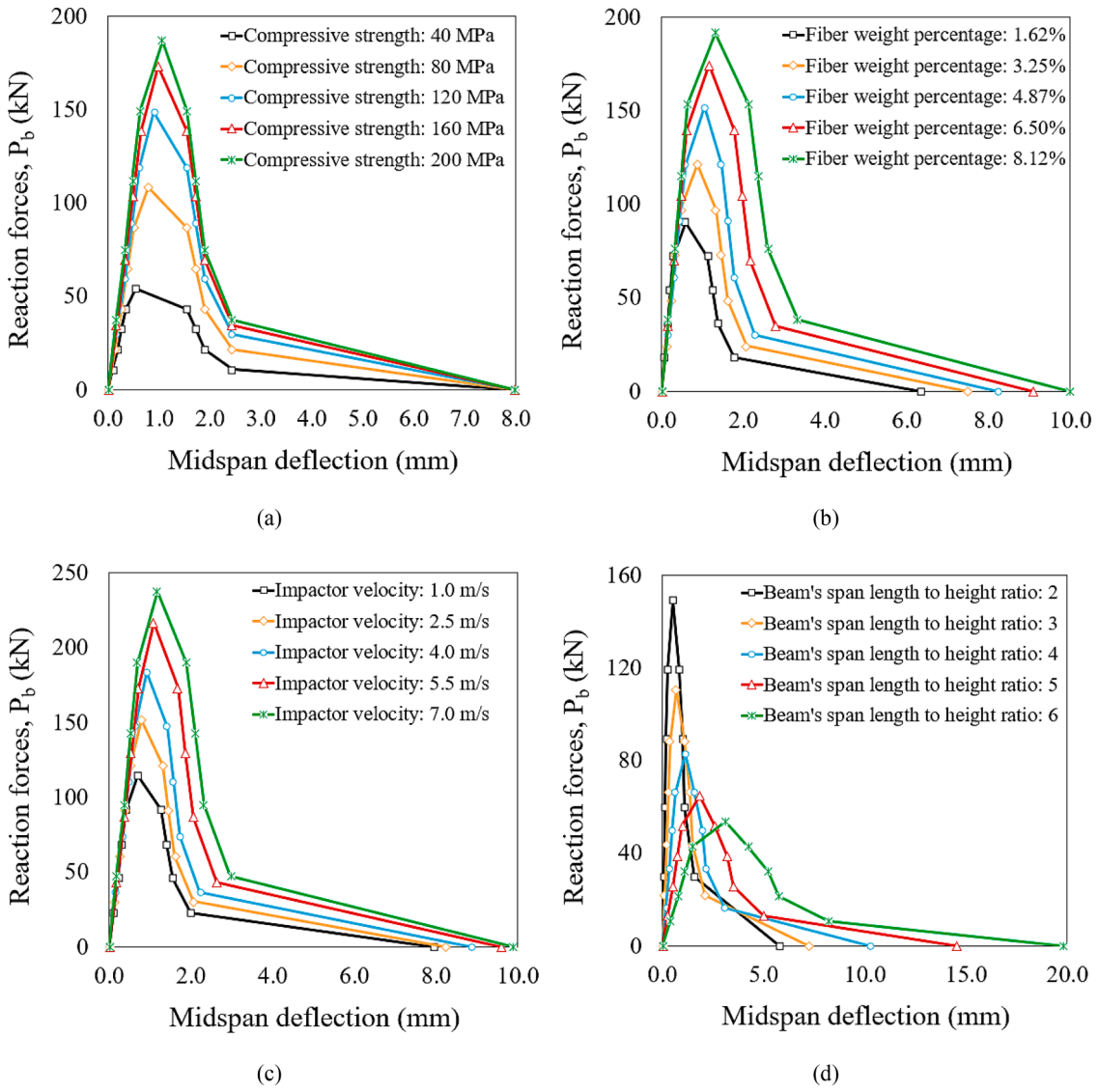


**Fig. 18.** Sensitivity analysis of reaction force-deflection curve due to (a) compressive strength; (b) fiber weight percentage; (c) impactor velocity; (d) beam's span length to height ratio.

**Table 4**
Input data of three specimens tested under drop weight impact by literature [11,15,23].

| ID type | $h$ [mm] | $b$ [mm] | $s$ [mm] | $l$ [mm] | $w_f$ [%] | Steel fiber shape | $\rho$ [kg.$m^{-3}$] | $f_{cm}$ [MPa] | $M$ [kg] | $H$ [mm] | $\dot{\delta}$ [mm.$s^{-1}$] |
|---|---|---|---|---|---|---|---|---|---|---|---|
| #1 by [11] | 150 | 150 | 50 | 500 | 1.67 | Prismatic | 2320 | 59 | 100 | 1750 | 5900 |
| #2 by [15] | 100 | 100 | 50 | 300 | 3.25 | Hooked | 2388 | 41 | 35 | 120 | 1470 |
| #3 by [23] | 150 | 150 | 100 | 500 | 3.98 | Hybrid* | 2408 | 114 | 121 | 360 | 2660 |

* Straight and hooked steel fibers.

sufficiently accurate. Fig. 20 illustrates a comparison between the experimental data and the predicted outcomes obtained from the proposed model. As it can be realized from the figures, the developed model predicts the peak impact force with an error that is less than 20%. Moreover, the best-fit lines for the predicted load of impactors is $P_{b,pre} = P_{b,exp}$ with R-squared of 0.82. As can be seen, in the lower range of values, corresponding to the lower strain rate, most of the predicted peak impact forces are higher than the experimental ones. When the value of impact force is increased, the model has a greater tendency to underestimate the results (Fig. 21a). Two main reasons can be behind this observation. First, the proposed simplified model is derived based on the energy-balance method, while with the increase of the impact force, the process of energy consumption becomes more complicated. It means that the energy-balance based model included some simplified assumption such as the linear acceleration distribution along the beam during impact process that influences the inertia force and subsequently the impact force. Furthermore, in the higher contact velocity between impactor and beam, the effective length of the beam might be changed, consequently the value of $V_s$ is different and the value of the displacement rate and strain rate are changed.

The proposed model estimates the minimum energy required to cause failure in an SFRC beam, based on its material properties and geometry, using Eq. (11b). In the present study, the mean absolute deviation (MAD) and mean absolute percentage error (MAPE) are used for

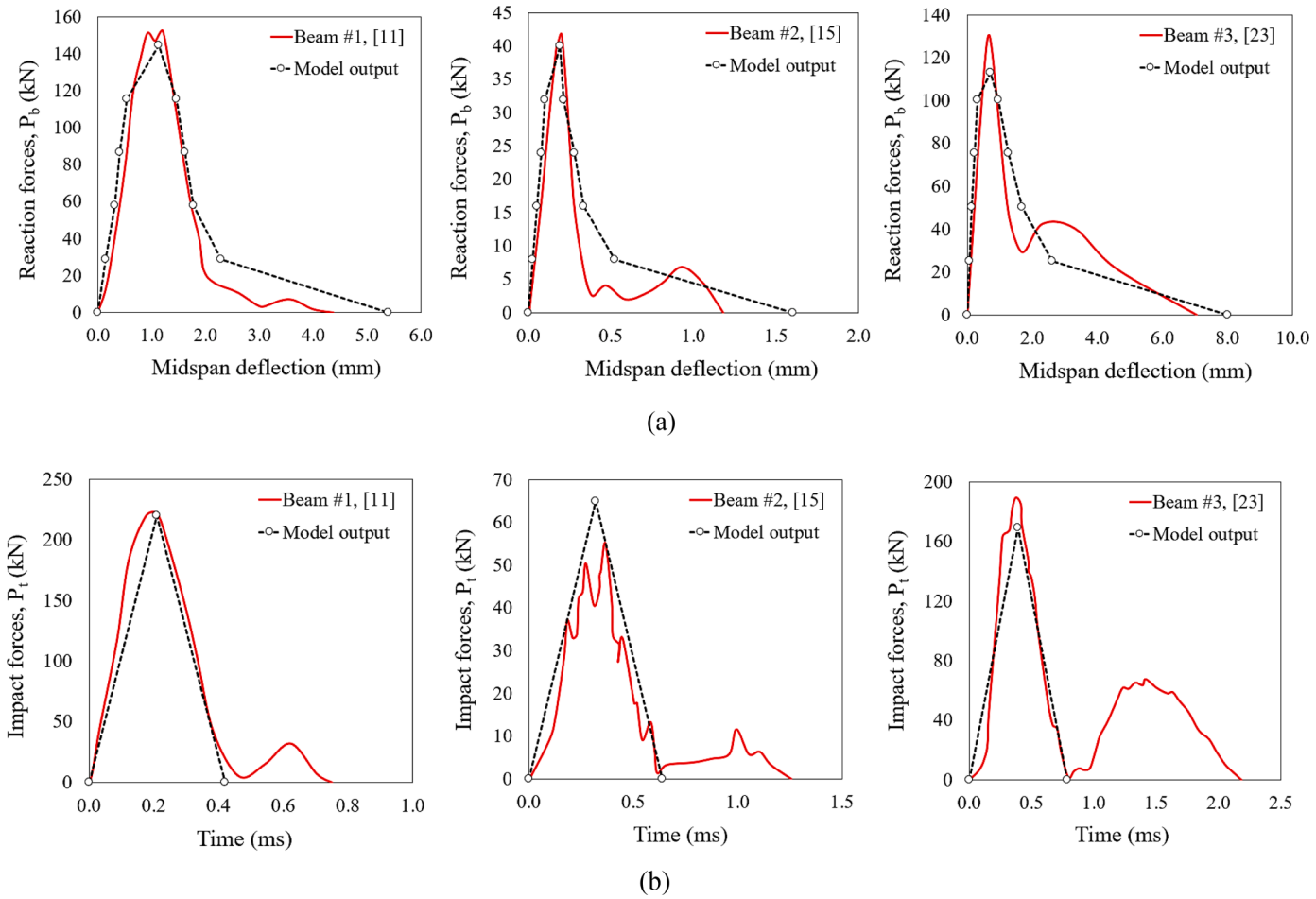


**Fig. 19.** Experimental and analytical (a) reaction forces-deflection responses; (b) impact force-time diagram.

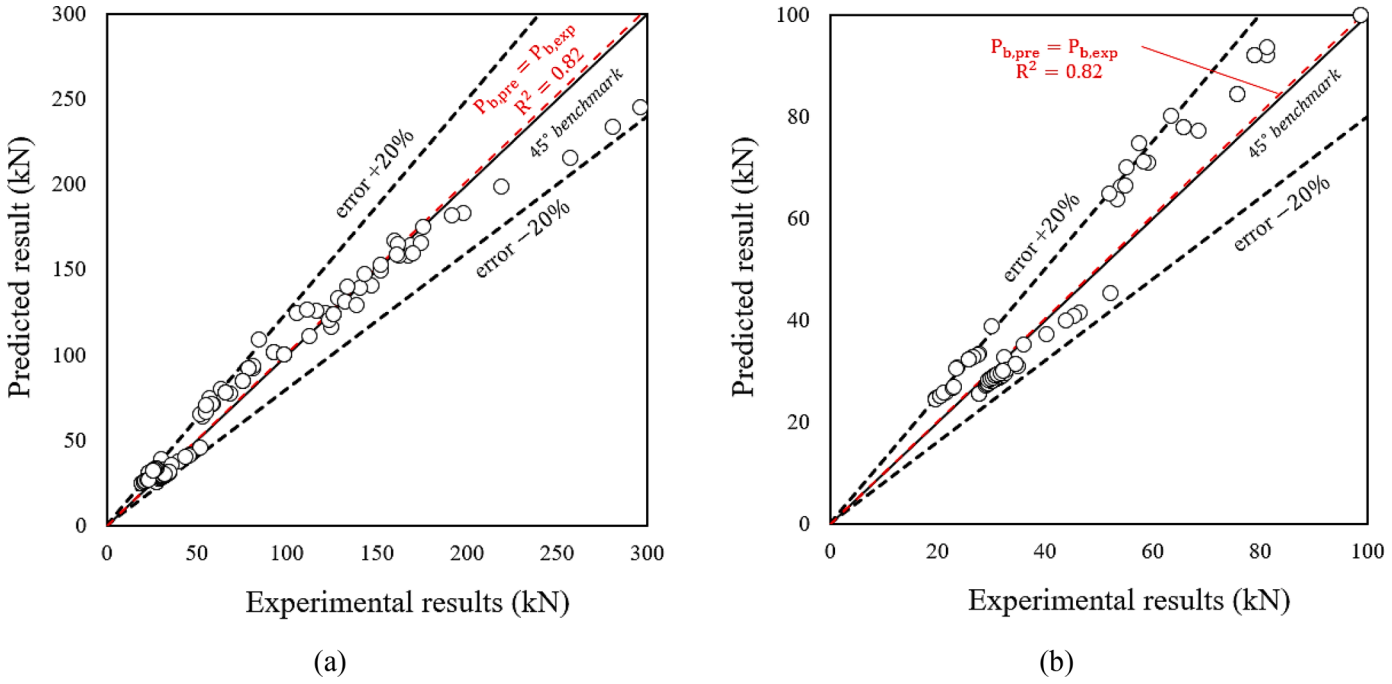


**Fig. 20.** Comparison of experimental and predicted values of maximum reaction force, $P_b$; (a) All results; (b) for $P_b < 100$ *kN*.

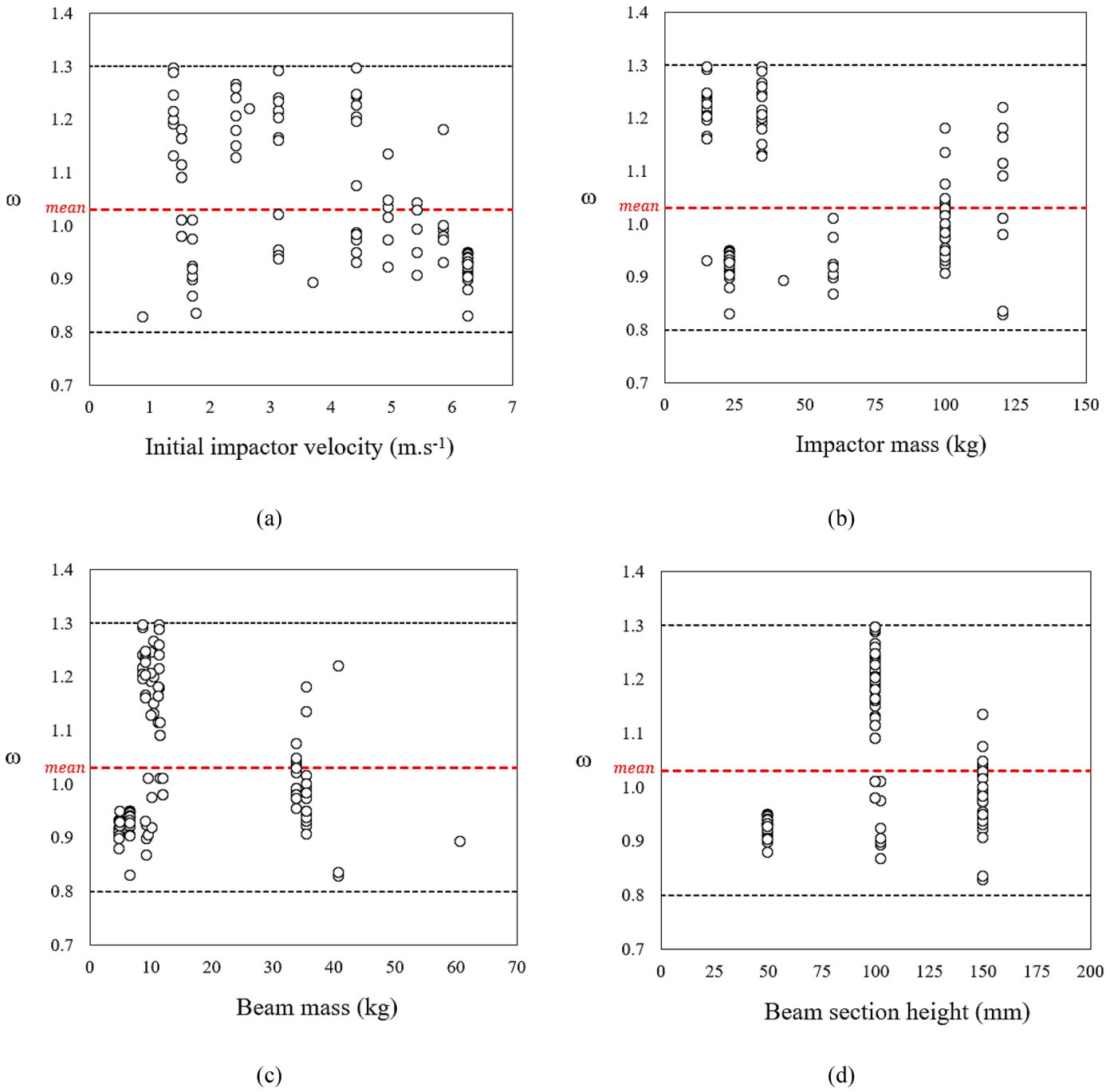


**Fig. 21.** Influence of the main parameters on $\omega$ (a) initial impactor velocity. (b) impactor mass; (c) beam mass; (d) beam height.

assessing the accuracy of the model.

$$MAD = \left(\frac{1}{N}\right)\sum_{1}^{N}|pre_i - exp_i| \tag{32}$$

$$MAPE = \left(\frac{1}{N}\right)\sum_{1}^{N}\left(\frac{pre_i - exp_i}{exp_i}\right) \tag{33}$$

where, *N*, *exp*, and *pre* are the total number of specimens, the experimental results, and the model predictions, respectively. The value of MAPE and MAD for the proposed model are 10% and 6.70, respectively. By increasing the number of data, it is expected that the precision of the model is enhanced. In addition, the predicted to experimental peak impact force ratio, $\omega$, is established. Subsequently a statistical analysis is conducted on $\omega$. The mean value of $\omega$ is 1.03 and its coefficient of variation is 0.13. The mass and velocity of impactor, the mass of the SFRC beam and the section height of the SFRC beam have been known as the physically significant parameters in predicting the peak impact response of the SFRC beam. The variation of $\omega$ with the mentioned parameters is shown in Fig. 21, and a value less than 1.3 was obtained. It means that the overall distribution of $\omega$ can be independent of the impact parameters. Consequently, the suggested model is able to be used for a wide range of these parameters.

## 4. Conclusion

- In the present study, a new analytical approach was proposed to predict the impact response of simply supported steel fiber

reinforced concrete (SFRC) beams using drop weight test. The proposed design methodology considers the theoretical basis derived from the impulse-momentum theorem and the principle of conservation of energy for calculating the maximum reaction force and the peak impact force. It also considers the moment-curvature response of a beam's cross-section under dynamic loading. This method assumes that the inertia force along the beam can be simulated by linear distribution. Using the conventional beam theory, a moment-curvature relationship is achieved in conjunction with a cross-section-layered approach. Then, the unit-load method is utilized to obtain the total beam's reaction forces-deflection relationship of the beam.

- The tensile and compressive behavior of concrete (the tensile strength and the mode-I fracture energy) are essential parameters in the flexural behavior of SFRC beams. Therefore, the effect of loading rate (strain rate) on the tensile and compressive behavior of SFRC was taken into account for calculating the moment-curvature response of a beam. The present study assumes that the tensile behavior of SFRC under high strain rate loading can be simulated by a bilinear diagram defining pre-cracking and post-cracking. Also, regarding the compressive behavior of SFRC, the strain rate affects the modulus of elasticity and the compressive strength.
- According to the impulse-momentum theorem and the principle of conservation of energy, the proposed model is able to predict the least amount of initial kinetic energy of impactor to fracture an SFRC beam and the impact loading time. Also, the velocity of the impactor after passing the SFRC beam can be calculated, which may be a beneficial parameter in anti-impact design. Subsequently, the maximum midspan deflection of SFRC beams under impact loading is determined considering the strain rate effect.
- Based on existing experimental results, the proposed model is applicable for various impactor mass and velocity combinations as well as for different geometries and masses of the beam. The accuracy of the proposed model in predicting the reaction forces of SFRC beams subjected to impact loading has been verified by comparing it to 121 experimental tests. Although the proposed model tends to slightly underestimate the reaction force of SFRC beams. The proposed model can be used for predicting the flexural behavior of SFRC under impact loading and also for simulating and design of SFRC beams under impact loading.

## CRediT authorship contribution statement

**Mohammad Bakhshi:** Conceptualization, Methodology, Software, Writing – original draft. **Joaquim A.O. Barros:** Writing – review & editing, Supervision. **Mohammadali Rezazadeh:** Conceptualization, Writing – review & editing. **Isabel B. Valente:** Validation, Writing – review & editing. **Honeyeh Ramezansefat:** Conceptualization, Writing – review & editing.

## Declaration of Competing Interest

The authors declare that they have no known competing financial interests or personal relationships that could have appeared to influence the work reported in this paper.

## Data availability

Data will be made available on request.

## Acknowledgements

The authors acknowledge the support provided by FCT through the project "FemWebAI - Integrated approach for reliable and advanced analysis and design of sustainable construction systems in fiber reinforced concrete", with reference PTDC/ECI-EST/6300/2020. The first author gratefully acknowledges the financial support of FCT for the Ph. D. Grant SFRH/BD/149246/2019.

## A. Calculating of beam's total reaction force-deflection diagram

According to the dynamic behavior of SFRC and beam geometry, the moment-curvature diagram is obtained. Then the force-deflection diagram can be derived from the moment-curvature curve of the SFRC beam as following steps:

**Step 1: Separating the moment-curvature curve to $2N$ discrete portions; assuming moment subdivision of $\Delta M$**

To define the moment-curvature diagram of the beam's midspan cross section with several points, the diagram is divided into two stages of pre- and post-peak, Fig. A1. The number of defined points before and after the peak is equal. From the moment-curvature diagram, a certain amount of curvature ($\chi_j$) can be derived for each moment value ($M_j$). In Fig. A1, $M_{pre}$ and $M_{post}$ show the bending moment at the pre-peak and post-peak stage, respectively, as well as $\chi_{pre}$ and $\chi_{post}$ show the curvature at the pre-peak and post-peak stage, respectively.

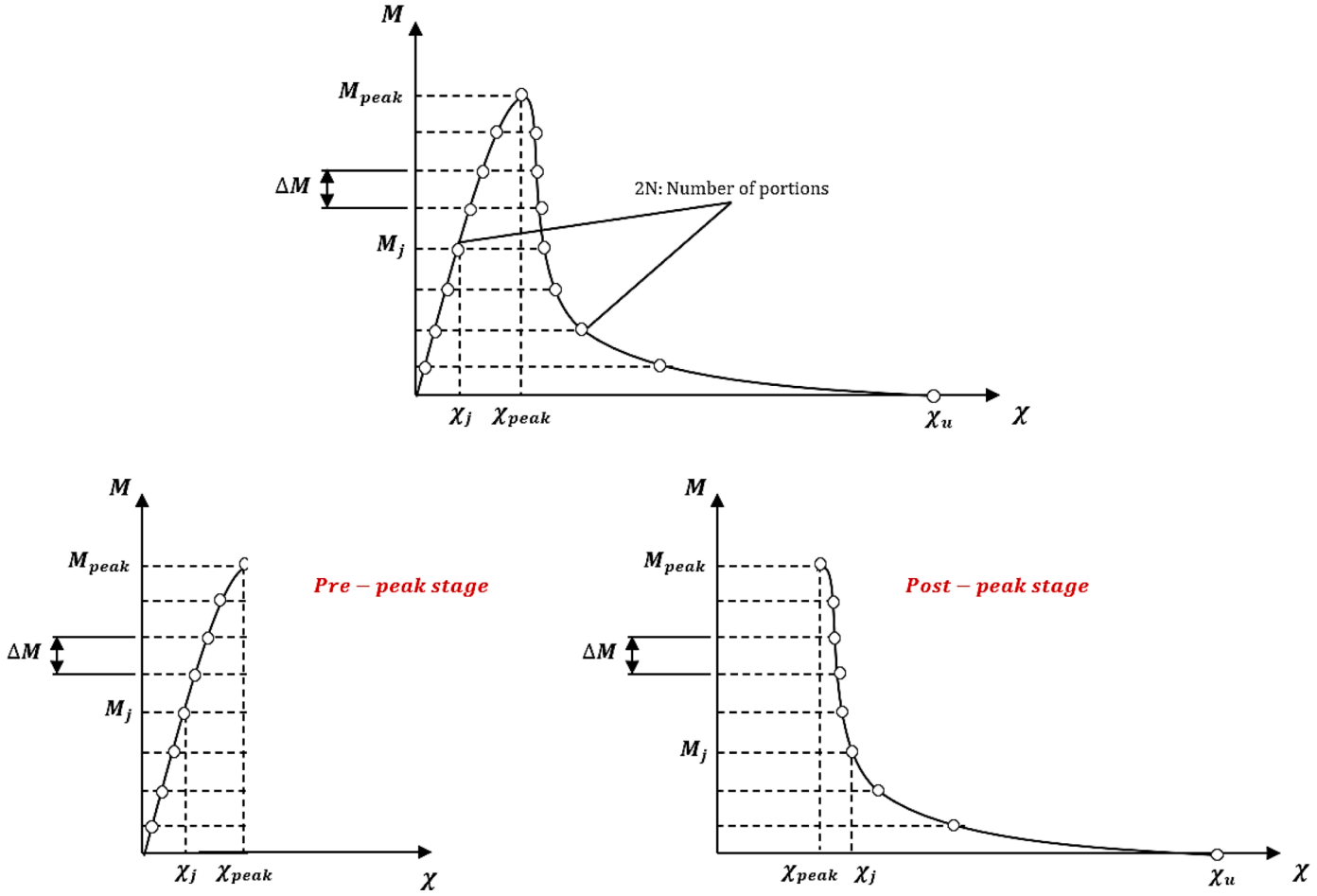


**Fig. A1.** Schematic discrete portions of moment-curvature curve.

$$M_j = \begin{bmatrix} M_{j,1} \\ M_{j,2} \\ . \\ . \\ M_{j,N} = M_{peak} \\ . \\ . \\ M_{j,2N} = 0 \end{bmatrix}_{2N\times 1} \rightarrow \quad \chi_j = \begin{bmatrix} \chi_{j,1} \\ \chi_{j,2} \\ . \\ . \\ \chi_{j,N} = \chi_{peak} \\ . \\ . \\ \chi_{j,2N} = \chi_u \end{bmatrix}_{2N\times 1} \tag{A1}$$

$$M_{pre} = \begin{bmatrix} M_{j,1} \\ M_{j,2} \\ . \\ . \\ . \\ M_{j,N} = M_{peak} \end{bmatrix}_{N\times 1} \rightarrow \quad \chi_{pre} = \begin{bmatrix} \chi_{j,1} \\ \chi_{j,2} \\ . \\ . \\ . \\ \chi_{j,N} = \chi_{peak} \end{bmatrix}_{N\times 1} \tag{A2}$$

$$M_{post} = \begin{bmatrix} M_{j,N+1} \\ . \\ . \\ . \\ M_{j,2N} = 0 \end{bmatrix}_{N\times 1} \rightarrow \quad \chi_{post} = \begin{bmatrix} \chi_{j,N+1} \\ . \\ . \\ . \\ \chi_{j,2N} = \chi_u \end{bmatrix}_{N\times 1} \tag{A3}$$

$$N = \frac{M_{peak}}{\Delta M} \tag{A4}$$

**Step 2: Calculation of the total reaction forces of the simply supported SFRC beam with overhang on both sides**

According to the Eq. (5a), the value of the total impact force ($P_t$) can be written in terms of the value of the moment at the beam's midspan [$M(s + l/2)$]. The reaction forces (sum of two supports force) is calculated based on the total inertia force in each loading step ($j$) replacing the value of $\psi$ by $\frac{P_i}{P_t}$, see Eqs. (1) and (6). Finally, the total reaction forces ($P_{b,j}$) correspond to each value of $M_j$ are obtained based on the $P_{i,j}$.

$$P_{b,j} = \left[\frac{12\left(l^2 - 4s^2\right)M_j - P_{i,j}\left(l^3 - 12s^2 l - 16s^3\right)}{3l\left(l^2 - 4s^2\right)}\right] \tag{A5}$$

The total inertia force ($P_i = P_{i,peak}$) calculated by Eq. (2) corresponds to $P_{b,peak}$. The $P_{i,j}$ shows the value of inertia force at each loading step which is obtained proportional to the $P_{b,j}$. It means that the value of $\psi$ is assumed constant during impact process.

$$\frac{P_{b,j}}{P_{b,peak}} = \frac{P_{i,j}}{P_{i,peak}} \tag{A6}$$

$$P_{b,peak} = \left[\frac{12\left(l^2 - 4s^2\right)M_{peak} - P_{i,peak}\left(l^3 - 12s^2 l - 16s^3\right)}{3l\left(l^2 - 4s^2\right)}\right] \tag{A7}$$

The Eq. (A5) can be written based on the $P_{b,j}$.

$$P_{b,j} = \left[\frac{12\left(l^2 - 4s^2\right)M_j.\ P_{b,peak}}{\left(P_{b,peak}\right)(3l)\left(l^2 - 4s^2\right) + \left(P_{i,peak}\right)\left(l^3 - 12s^2 l - 16s^3\right)}\right] \tag{A8}$$

The value of $P_{b,j}$ represents the Y-axis of the reaction force-deflection diagram and $P_{b,peak}$ corresponds to $M_{peak}$. This means that for each point defined in the moment-curvature diagram, a corresponding point in the force-displacement diagram is obtained.

**Step 3: Separating the length of the beam to $2N^{'}$ discrete portions; assuming length subdivision of $\Delta x$.** Figs. A2 and A3

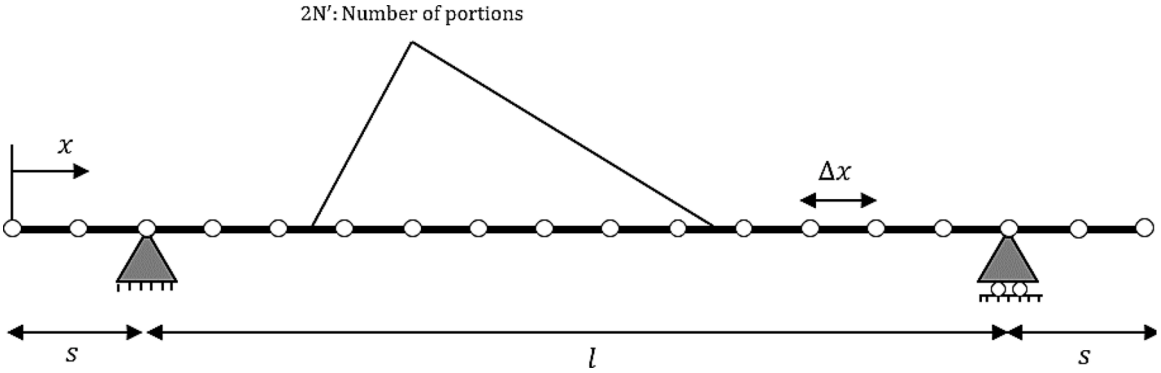


**Fig. A2.** Schematic discrete portions of beam length.

$$0 \le x \le s + \frac{l}{2}; \qquad 2N^{'} = \frac{l + 2s}{\Delta x}; \qquad x_i = 0; \Delta x; s + \frac{l}{2} \tag{A9}$$

According to the division made for the length of the beam and the moment-curvature diagram, as well as the relationship of the bending moment distribution along the length of the beam, for each moment in the moment-curvature diagram ($M_j$ at beam's midspan), the value of the moment at all points along the length of the beam can be calculated.

$$m\left(x, M_j\right) = \begin{cases} \left[\dfrac{2P_{i,j}}{3\left(l^2 - 4s^2\right)}\right]\left(x^3 - 3sx^2\right), & 0 \le x < s \\ \left[\dfrac{2P_{i,j}}{3\left(l^2 - 4s^2\right)}\right]\left(x^3 - 3sx^2\right) + \left(\dfrac{P_{b,j}}{2}\right)(x - s), & s \le x \le s + \dfrac{l}{2} \end{cases} \tag{A10}$$

The values of $\Delta m^{'}$ and $\Delta m$ show the difference between the peak moment ($M_{peak}$) and the moment at the beam's midspan ($M_j$) and the other points of the beam [$m(x, M_j)$] at the post-peak stage, respectively. These values are used for calculating the midspan deflection at the post-peak stage.

$$\Delta m\left(x, M_j\right) = M_{peak} - m\left(x, M_j\right); \qquad \Delta m^{'} = M_{peak} - M_{post} \tag{A11}$$

$$\Delta m^{'} = \begin{bmatrix} M_{peak} - M_{j,N+1} = \Delta M \\ M_{peak} - M_{j,N+2} = 2 \times \Delta M \\ \vdots \\ M_{peak} - M_{j,2N} = N \times \Delta M = M_{peak} \end{bmatrix}_{N \times 1} \tag{A12}$$

**Step 4: Calculation of the midspan deflection due to bending moment**

To calculate the $\delta_{mj}$, the unit-load method (or conjugate-beam) is used ($\delta_m = \int_0^l \frac{M_{un}.M_l}{EI} dx$). For this purpose, firstly, the $M - \chi$ diagram is divided into two stages of pre- and post-peak, Fig. A1. At the pre-peak stage ($\chi_j \le \chi_{peak}$ or $j \le N$), based on the distribution of the moment along the beam [see Eq. (5a)], the distribution of curvature can be obtained (see Step 1). By using the unit-load method (or conjugate-beam) and considering the curvature as the applied load ($\chi_j \le \chi_{peak}$), the value of the moment at the midspan of the conjugate-beam is equal to the midspan deflection of the original-beam ($\delta_{mj}$). This means that for each value of $M_j$ in the pre-peak stage, $\delta_{mj}$ is calculated. This concept can be expressed as the following relationship.

$$\frac{d^2\delta_{mj}}{dx^2} = \frac{m\left(x, M_j\right)}{EI}; \quad \delta_{mj} = \int\int \left[\frac{m\left(x, M_j\right)}{EI}\right] dx^2 \tag{A13}$$

$$\delta_{mj} = \int_0^{s+l/2} linterp\left[M_{pre}, \chi_{pre}, m(x, M_j)\right].x.dx; \qquad j \le N \tag{A14}$$

Regards to post-peak stage ($\chi_j > \chi_{peak}$ or $N < j \le 2N$), it is assumed that the beam's midspan will follow the softening portion of the $M-\chi$ relationship. While the other sections of the beam entered in an unloading stage with slope of $(EI)_{sec} = M_{peak}/\chi_{peak}$. As a result, although the amount of $M_j$ (and $P_{bj}$) decreases at the beam's midspan, the amount of $\chi_j$ (and $\delta_{mj}$) increases, see Section 2.3.4 Beam's reaction forces-deflection diagram. The difference between the post-peak curvature ($\chi_j$) and $\chi_{peak}$ in the original-beam's midspan is considered as a point load in the conjugate-beam's midspan. In this case, the moment value in the conjugate-beam's midspan (with uniformly distributed loading due to the uniformly distributed curvature in the original-beam and a point load in the beam's midspan due to the $(\chi_j - \chi_{peak}).2\Delta x$) would be equivalent to its deflection in the original-beam. The $\delta_{mj}$ for the post-peak stage can be calculated by follow equation.

$$\delta_{mj} = \left[\int_0^{s+l/2} linterp\left(M_{pre}, \chi_{pre}, m(x, M_j)\right).x.dx\right] + \left[linterp\left(\Delta m', \chi_{post}, \Delta m\left(s+\frac{l}{2}, M_j\right)\right)\right] \times \frac{l}{2}; \quad j > N \tag{A13}$$

Eq. (A11) includes two terms that the first and second terms show the beam's midspan deflection due to the uniformly distributed curvature along entire beam and the point load in the beam's midspan, respectively.

**Step 5: Calculation of the midspan deflection due to shear force**

To calculate the $\delta_{vj}$, the unit-load method (or conjugate-beam) is used ($\delta_v = \int_0^l \frac{V_{un}.V_l}{GA.f_{sh}} dx$). At any stage throughout the loading process of the beam, shear strains on the $V-\gamma$ linear response (see Fig. 14a) are calculated by dividing the shear force by the shearing rigidity ($GAf_{sh}$). This means that in the pre-peak stage, the effect of shear forces on deflection increases up to $P_{peak}$, then its effect decreases with increasing deflection in the post-peak stage. It is worth noting that the shear force at each point of the beam ($V_j$) can be obtained by Eq. (5a). The value of $V_j$ at the beam's midspan can be obtained by replacing $(s + l/2)$ by $x$ in Eq. (5a).

$$V_j = \frac{P_{bj}}{2} \tag{A14}$$

By using the unit-load method (or conjugate-beam) and considering the shear strain as the applied load, the value of the shear at the midspan of the conjugate-beam is equal to the midspan deflection of the original-beam ($\delta_{vj}$).

$$\delta_{vj} = \frac{V_j}{G.A.f_{sh}} \int_s^{s+l/2} 1.dx = \frac{P_{bj}.l}{4Gbhf_{sh}} \tag{A15}$$

Finally, since the effects of shear and moment on midspan deflection were calculated separately, the superposition concept was used to calculate the total deflection as the sum of both effects ($\delta_{vj}$ and $\delta_{mj}$).

$$\delta_j = \delta_{mj} + \delta_{vj} \tag{A16}$$

The value of $\delta_j$ represents the X-axis of the reaction force-deflection diagram and $\delta_{peak}$ corresponds to $P_{peak}$. Considering both effect of shear force and moment on the deflection at the beam's midspan, the reaction force-deflection responses is obtained for simply supported SFRC beam. The impact force-deflection response is determined based on the force equilibrium in the simply supported SFRC beam ($P_t = P_i + P_b = \frac{P_b}{(1-\psi)}$). As a result, the technique adopted is thought to be adequately precise. Care must be taken when using this method to calculate the force-deflection response for beams with different loading configurations.

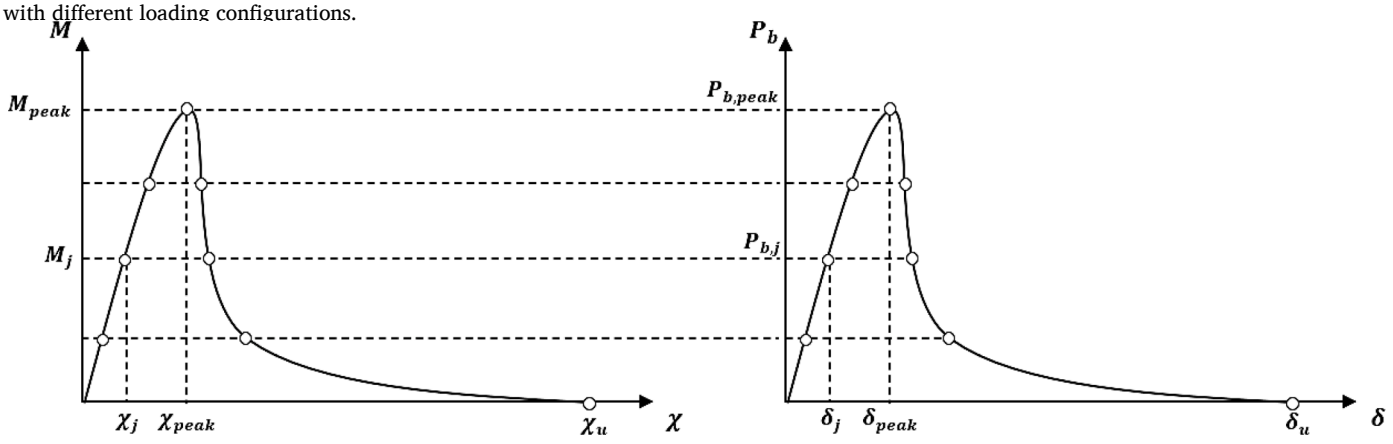


**Fig. A3.** Schematic reaction force-deflection ($P_b - \delta$) diagrams for the simply supported SFRC beam.

## B. Example from literature (Zhang et al. [23]) for obtaining impact response of SFRC beam

### B.1 Input data for the analytical model Table B1

**Table B1**
Input data for the analytical model.

| $h$ [mm] | $b$ [mm] | $l$ [mm] | $s$ [mm] | $f_{sh}$ | $f_{cm}$ [MPa] | $w_f$ [%] | $\rho$ [kg.$m^{-3}$] | $m$ [kg] | $H$ [mm] | $\upsilon$ |
|---|---|---|---|---|---|---|---|---|---|---|
| 150 | 150 | 500 | 100 | 5/6 | 114 | 1.23 | 2408 | 120.6 | 360 | 0.2 |

### B.2 Loading and beam's test setup Fig. B1

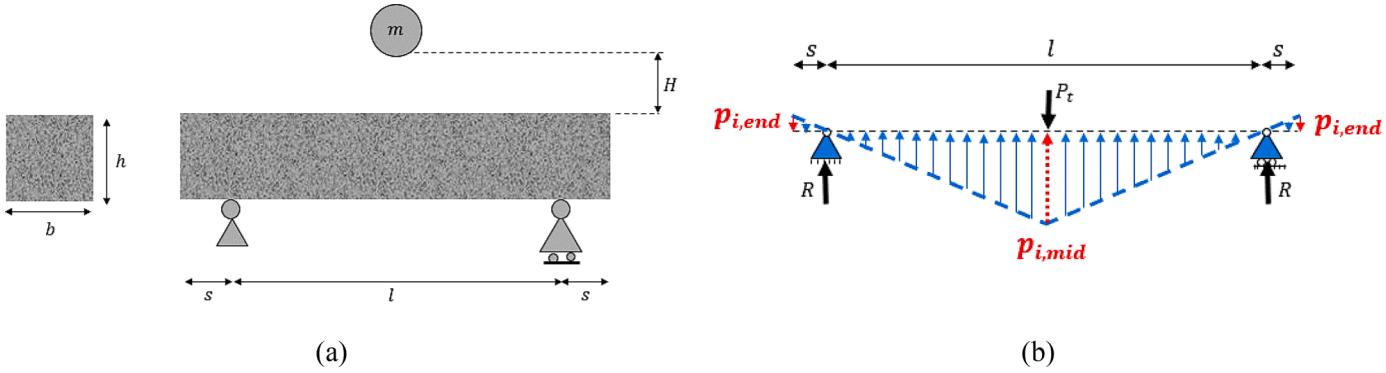


**Fig. B1.** (a) Beam's test setup; (b) Loading condition.

### B.3 Calculating the maximum acceleration and total inertia force, Eqs. (2) – (7) Table B2

**Table B2**
Calculating the maximum acceleration and total inertia force.

| $E$ [MPa] | $A$ [$mm^2$] | $I$ [$mm^4$] | $k$ [N.$m^{-1}$] | $k_2$ | $H_2$ | $H_3$ | $\ddot{\delta}_{max}$ [m.$s^{-2}$] | $P_i$ [kN] | $P_{i,mid}$ [kN] | $P_{i,end}$ [kN] |
|---|---|---|---|---|---|---|---|---|---|---|
| 48,388 | 22,500 | 4.2E+07 | 7.8E+08 | 1 | 1 | 0 | 5953 | 56.1 | 267.2 | 106.9 |

### B.4 Calculating the quasi-static compressive and tensile behavior of SFRC, Eqs. (19a) – (23a) Table B3 and Fig. B2

**Table B3**
Input data to adopt the quasi-static stress-strain relation of SFRC materials.

| $E_c$ [MPa] | $p$ | $q$ | $\varepsilon_{cl}$ | $p_2$ | $p_1$ | $\alpha$ | $\varepsilon_{cr}$ | $G_F$ [N.$m^{-1}$] | $G_{Ff}$ [N.$m$−1] | $D_{max}$ [mm] | $l_b$ [mm] | $g_{Ff}$ [kN.$m$ − 2] | $f_{ctm}$ [MPa] |
|---|---|---|---|---|---|---|---|---|---|---|---|---|---|
| 48,388 | 0.43 | −0.39 | 2.45E-03 | 598 | 1.1 | 0.4 | 1.40E-04 | 171.2 | 4093.1 | 12 | 36 | 113.7 | 6.76 |

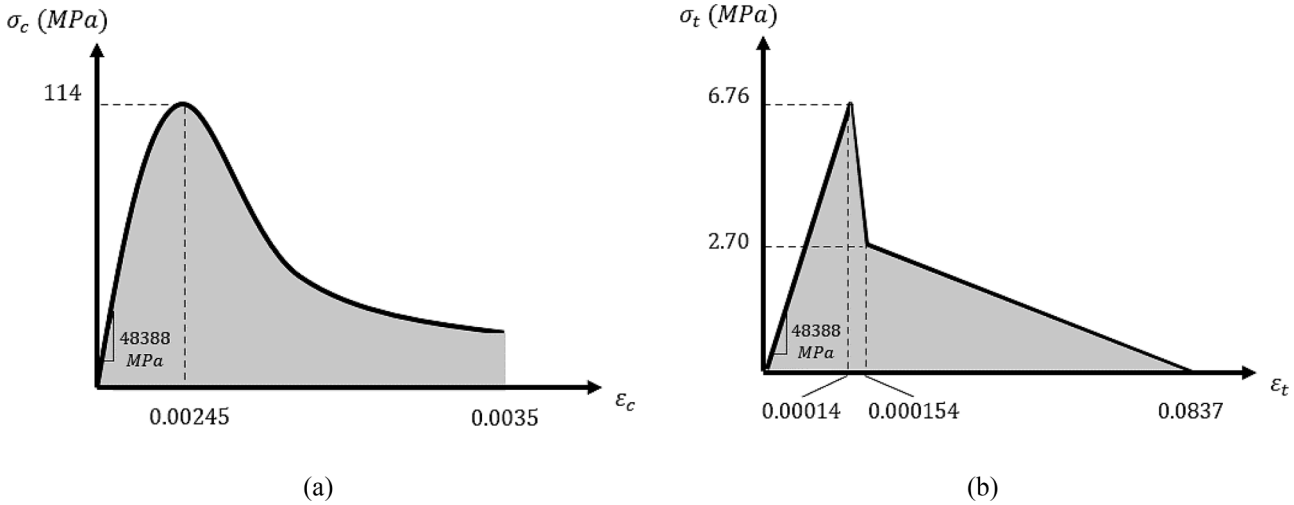


**Fig. B2.** Quasi-static stress-strain relation for SFRC in (a) Compression; (b) Tension.

### B.5 Calculating the dynamic compressive and tensile behavior of SFRC, Eqs. (24) – (30) Table B4 and Fig. B3

**Table B4**
Input data to adopt the dynamic stress-strain relation of SFRC materials.

| $m'$ [kg] | $V_c$[m.$s^{-1}$] | $V_s$[m.$s^{-1}$] | $\dot{\delta}_d$[mm.$s^{-1}$] | $\dot{\varepsilon}_c$[$s^{-1}$] | $\dot{\varepsilon}_t$[$s^{-1}$] | $E_{c,dy}$ [MPa] | $f_{cm,dy}$ [MPa] | $f_{ctm,dy}$ [MPa] | $DIF_G$ | $G_{Ff,dy}$ [N.$m^{-1}$] | $g_{Ff,dy}$ [kN.$m^{-2}$] | $\xi$ |
|---|---|---|---|---|---|---|---|---|---|---|---|---|
| 37.9 | 2.7 | 2.0 | 2022.1 | 7.28 | 7.28 | 66,795 | 135.6 | 15.99 | 1.94 | 7928.4 | 220.2 | 116.1 |

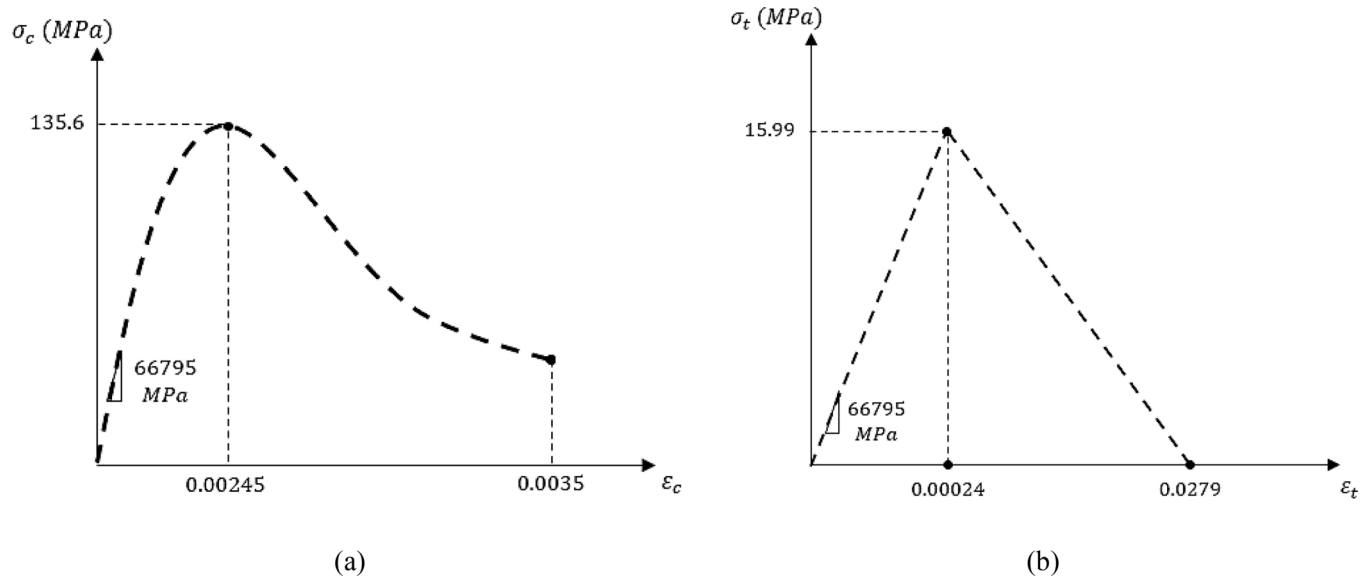


**Fig. B3.** Dynamic stress-strain relation for SFRC in (a) Compression; (b) Tension.

### B.6 Deriving the moment-curvature diagram from the sectional analysis by DOCROS[46] Fig. B4

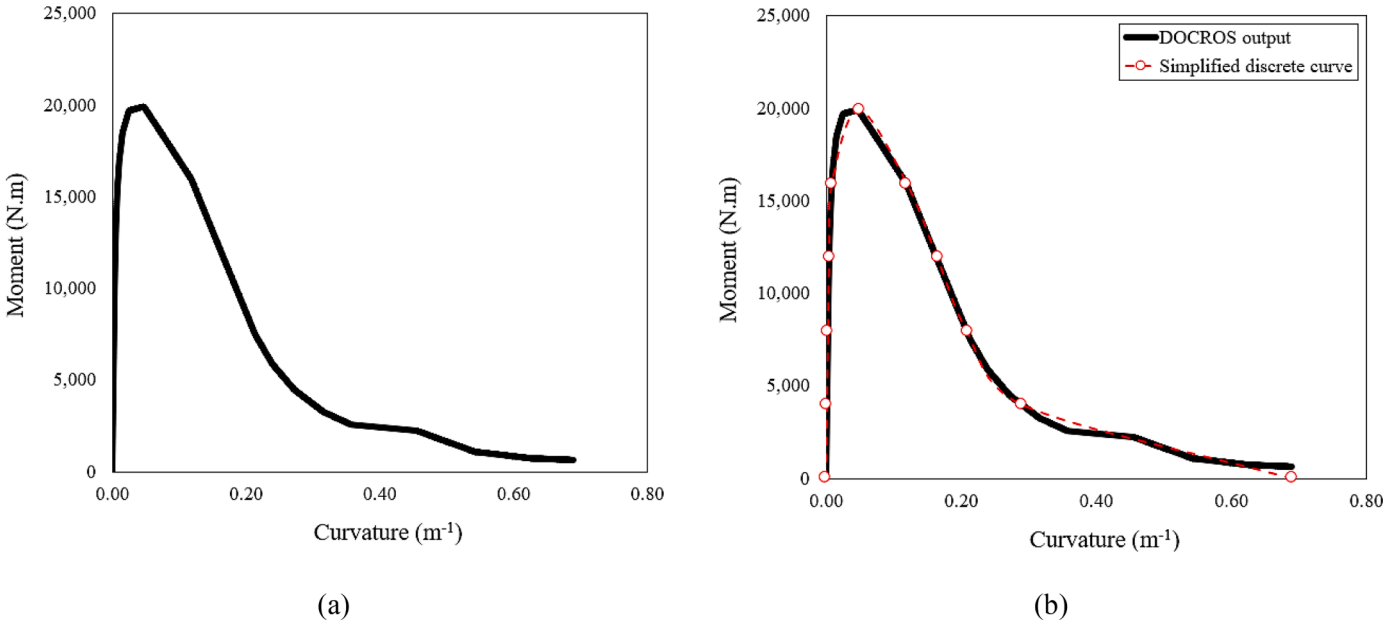


**Fig. B4.** Moment-curvature curve; (a) DOCROS output; (b) Simplifying to discrete points ($2N = 10$).

### B.7 Beam's reaction forces-deflection diagram using the unit-load method (or conjugate-beam), Eq. (31) Tables B5 and B6

**Table B5**
The values of moment and curvature at each point of curve ($2N = 10$, $\Delta M = 3983$ N.m).

| Stage | Pre-peak | | | | Post-peak | | | | | |
|---|---|---|---|---|---|---|---|---|---|---|
| $1 \le j \le 2N$ | 1 | 2 | 3 | 4 | 5 | 6 | 7 | 8 | 9 | 10 |
| $\chi_j$ [$m^{-1}$] | 1.43E-03 | 2.84E-03 | 4.57E-03 | 8.55E-03 | 4.80E-02 | 1.20E-01 | 1.64E-01 | 2.08E-01 | 2.90E-01 | 6.89E-01 |
| $M_j$ [N.m] | 3.39E+03 | 6.77E+03 | 1.02E+04 | 1.35E+04 | 1.52E+04 | 1.35E+04 | 1.02E+04 | 6.77E+03 | 3.39E+03 | 0.00E+00 |

**Table B6**
The values of reaction forces $P_{b,j}$ based on each value of $M_j$.

| Stage | Pre-peak | | | | Post-peak | | | | | |
|---|---|---|---|---|---|---|---|---|---|---|
| $1 \le j \le 2N$ | 1 | 2 | 3 | 4 | 5 | 6 | 7 | 8 | 9 | 10 |
| $P_{i,j}$ [kN] | 12.47 | 24.95 | 37.42 | 49.89 | 56.10 ($P_{i,peak}$) | 49.89 | 37.42 | 24.95 | 12.47 | 0.00 |
| $P_{b,j}$ [kN] | 25.14 | 50.29 | 75.43 | 100.58 | 113.10 ($P_{b,peak}$) | 100.58 | 75.43 | 50.29 | 25.14 | 0.00 |

The value of 0.33 was obtained for $\psi$that is constant during impact loading. Fig. B5 and Tables B7 and B8

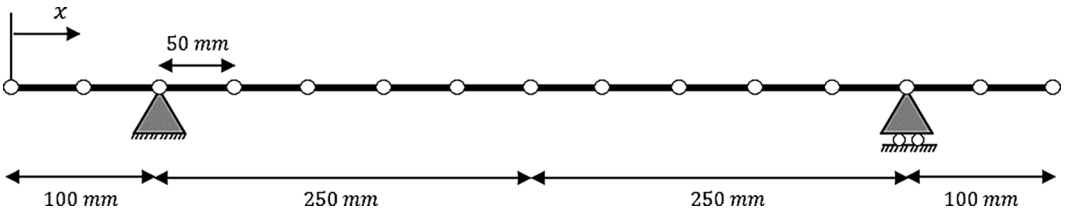


**Fig. B5.** Separating the beam's length to $2N^{'} = 14$ discrete portions; assuming length subdivision of $\Delta x = 50\ mm$.

**Table B7**
The value of $m(x, M_j)$ at the pre-peak stage.

| $0 \le x \le s + l/2$ [mm] | $1 \le j \le N$ | | | | |
|---|---|---|---|---|---|
| | 1 | 2 | 3 | 4 | 5 |
| 0 | 0.00E+00 | 0.00E+00 | 0.00E+00 | 0.00E+00 | 0.00E+00 |
| 50 | −2.47E+01 | −4.95E+01 | −7.42E+01 | −9.90E+01 | −1.11E+02 |
| 100 | −7.92E+01 | −1.58E+02 | −2.38E+02 | −3.17E+02 | −3.56E+02 |
| 150 | 4.95E+02 | 9.90E+02 | 1.48E+03 | 1.98E+03 | 2.23E+03 |
| 200 | 1.10E+03 | 2.20E+03 | 3.30E+03 | 4.40E+03 | 4.94E+03 |
| 250 | 1.76E+03 | 3.52E+03 | 5.29E+03 | 7.05E+03 | 7.93E+03 |
| 300 | 2.51E+03 | 5.03E+03 | 7.54E+03 | 1.01E+04 | 1.13E+04 |
| 350 (midspan) | 3.39E+03 | 6.77E+03 | 1.02E+04 | 1.35E+04 | 1.52E+04 |

**Table B8**
The value of $m(x, M_j)$ at the post-peak stage.

| $0 \le x \le s + l/2$ [mm] | $N+1 \le j \le 2N$ | | | | |
|---|---|---|---|---|---|
| | 6 | 7 | 8 | 9 | 10 |
| 0 | 0.00E+00 | 0.00E+00 | 0.00E+00 | 0.00E+00 | 0.00E+00 |
| 50 | −9.90E+01 | −7.42E+01 | −4.95E+01 | −2.47E+01 | 0.00E+00 |
| 100 | −3.17E+02 | −2.38E+02 | −1.58E+02 | −7.92E+01 | 0.00E+00 |
| 150 | 1.98E+03 | 1.48E+03 | 9.90E+02 | 4.95E+02 | 0.00E+00 |
| 200 | 4.40E+03 | 3.30E+03 | 2.20E+03 | 1.10E+03 | 0.00E+00 |
| 250 | 7.05E+03 | 5.29E+03 | 3.52E+03 | 1.76E+03 | 0.00E+00 |
| 300 | 1.01E+04 | 7.54E+03 | 5.03E+03 | 2.51E+03 | 0.00E+00 |
| 350 (midspan) | 1.35E+04 | 1.02E+04 | 6.77E+03 | 3.39E+03 | 0.00E+00 |

It should be noted that due to symmetry in geometry and loading, $m(x, M_j)$ at half the beam's length was calculated which can be used for the other half of the beam as well. According to $M - \chi$ diagram, the value of curvature along the beam [$\chi(x,M_j)$] for each value of midspan moment $M_j$ in the pre-peak stage is obtained. Table B9

**Table B9**
The value of $\chi(x, M_j)$ at the pre-peak stage.

| $0 \le x \le s + l/2$ [mm] | $1 \le j \le N$ | | | | |
|---|---|---|---|---|---|
| | 1 | 2 | 3 | 4 | 5 |
| 0 | 0.00E+00 | 0.00E+00 | 0.00E+00 | 0.00E+00 | 0.00E+00 |
| 50 | 9.37E-06 | 1.87E-05 | 2.81E-05 | 3.75E-05 | 4.69E-05 |
| 100 | 3.00E-05 | 6.00E-05 | 9.00E-05 | 1.20E-04 | 1.50E-04 |
| 150 | 2.66E-04 | 5.33E-04 | 7.99E-04 | 1.07E-03 | 1.33E-03 |
| 200 | 5.74E-04 | 1.15E-03 | 1.72E-03 | 2.29E-03 | 2.86E-03 |
| 250 | 9.04E-04 | 1.81E-03 | 2.71E-03 | 3.66E-03 | 4.76E-03 |
| 300 | 1.27E-03 | 2.53E-03 | 3.89E-03 | 5.49E-03 | 9.03E-03 |
| 350 (midspan) | 1.68E-03 | 3.35E-03 | 5.38E-03 | 1.01E-02 | 5.65E-02 |

Regards to post-peak stage, it is assumed that the beam's midspan will follow the softening portion of the $M-\chi$ relationship. While the other sections of the beam entered in an unloading stage with slope of $(EI)_{sec} = M_{peak}/\chi_{peak}$. Table B10, Fig. B6 and B7 and Table B11

**Table B10**
The value of $\chi(x, M_j)$ at the post-peak stage.

| $0 \le x \le s+l/2$ [mm] | $N+1 \le j \le 2N$ | | | | |
|---|---|---|---|---|---|
| | 6 | 7 | 8 | 9 | 10 |
| 0 | 0.00E+00 | 0.00E+00 | 0.00E+00 | 0.00E+00 | 0.00E+00 |
| 50 | 3.67E-04 | 2.75E-04 | 1.84E-04 | 9.18E-05 | 0.00E+00 |
| 100 | 1.17E-03 | 8.81E-04 | 5.87E-04 | 2.94E-04 | 0.00E+00 |
| 150 | 7.34E-03 | 5.51E-03 | 3.67E-03 | 1.84E-03 | 0.00E+00 |
| 200 | 1.63E-02 | 1.22E-02 | 8.15E-03 | 4.07E-03 | 0.00E+00 |
| 250 | 2.61E-02 | 1.96E-02 | 1.31E-02 | 6.53E-03 | 0.00E+00 |
| 300 | 3.73E-02 | 2.80E-02 | 1.86E-02 | 9.32E-03 | 0.00E+00 |
| 350 (midspan) | 1.20E-01 | 1.64E-01 | 2.08E-01 | 2.90E-01 | 6.89E-01 |

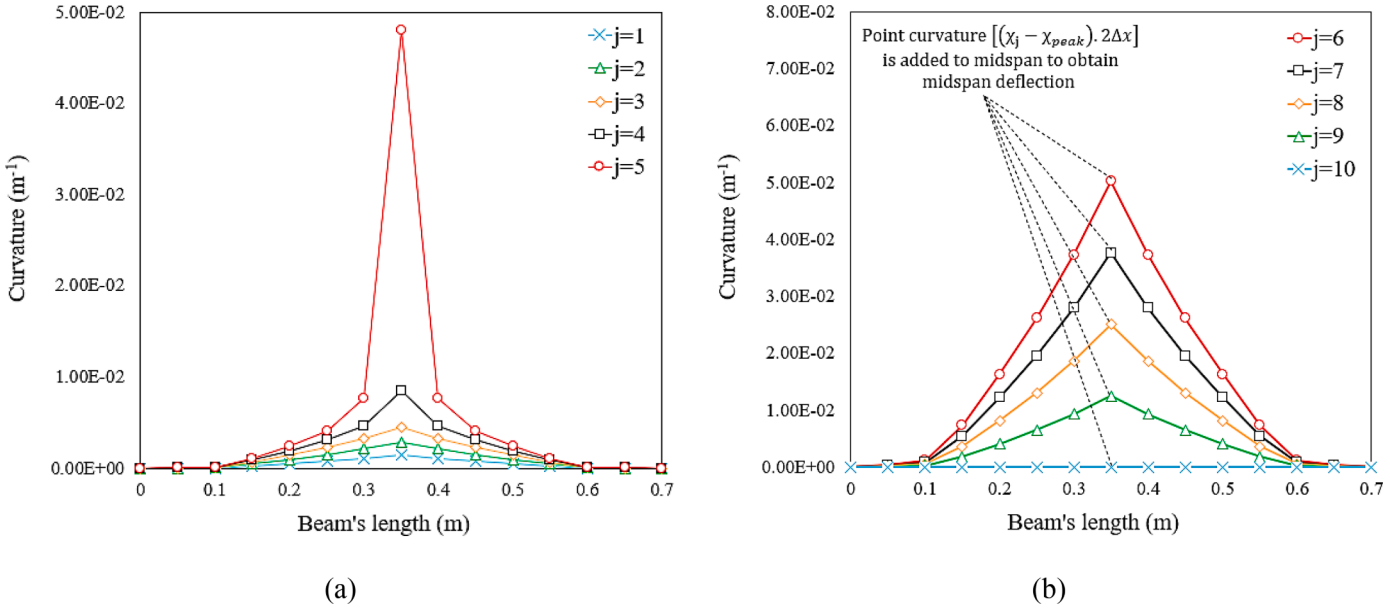


**Fig. B6.** Curvature distribution along the beam's length; (a) at pre-peak stage; and (b) at post-peak stage.

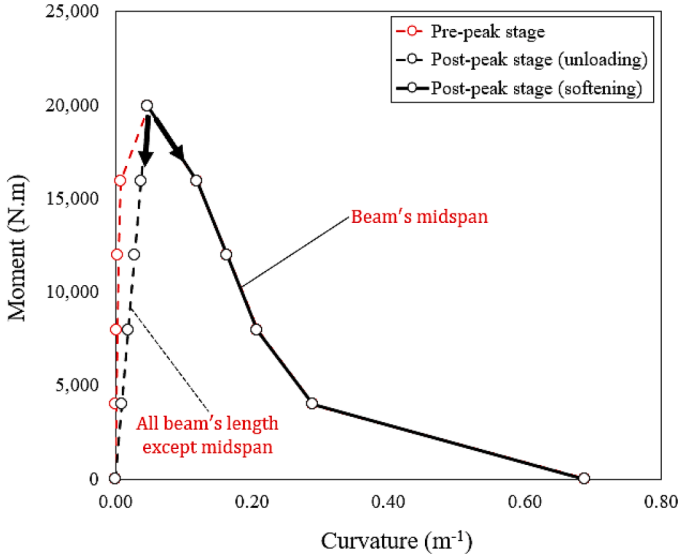


**Fig. B7.** Post-peak stage of moment-curvature.

**Table B11**
The values of deflection due to moment, $\delta_{m,j}$, and due to shear, $\delta_{v,j}$.

| Stage | Pre-peak | | | | Post-peak | | | | | |
|---|---|---|---|---|---|---|---|---|---|---|
| $1 \leq j \leq 2N$ | 1 | 2 | 3 | 4 | 5 | 6 | 7 | 8 | 9 | 10 |
| $\delta_{m,j}$ [mm] | 6.25E-02 | 1.25E-01 | 1.91E-01 | 2.79E-01 | 6.77E-01 ($\delta_{m,peak}$) | 9.29E-01 | 1.24E+00 | 1.66E+00 | 2.61E+00 | 8.02E+00 |
| $\delta_{v,j}$ [mm] | 8.31E-03 | 1.66E-02 | 2.49E-02 | 3.33E-02 | 3.74E-02 ($\delta_{v,peak}$) | 3.33E-02 | 2.49E-02 | 1.66E-02 | 8.31E-03 | 0.00E+00 |
| $\delta_j$ [mm] | 7.08E-02 | 1.41E-01 | 2.16E-01 | 3.13E-01 | 7.15E-01 ($\delta_{peak}$) | 9.62E-01 | 1.27E+00 | 1.67E+00 | 2.62E+00 | 8.02E+00 |

Since the analyzed specimen from literature (Zhang et al. [23]) was completely fractured under impact loading, the analytical reaction forces-midspan diagram can be compared to the experimental results. Fig. B8

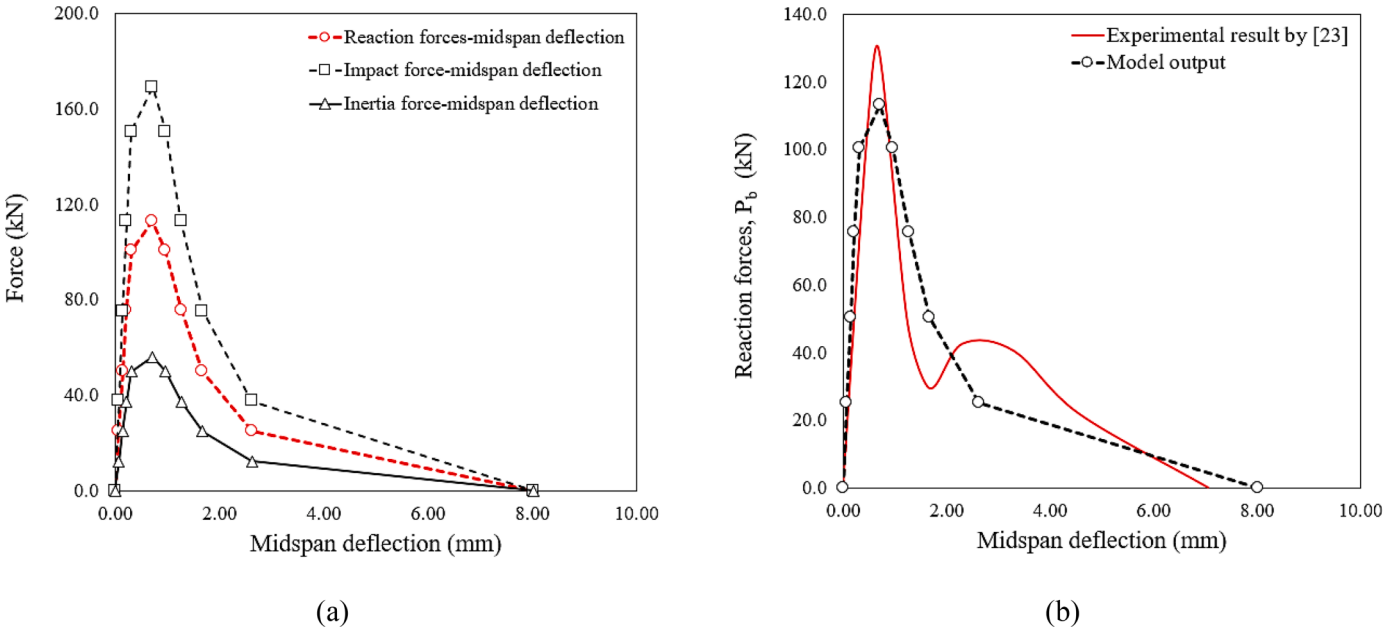


**Fig. B8.** (a) Reaction forces- and impact force-midspan deflection diagram; (b) Comparison between the experimental (Zhang et al. [23]) and analytical results.

**B.8 Calculation of the impact response of SFRC beam ($P_t$) under drop-weight impact using energy-balance based model**, Eqs. (8) – (18b) Table B12 and Fig. B9

**Table B12**
Proposed energy-balance based model.

| $E_{cap.}$ [J] | $\delta_u$ [mm] | $U$ [J] | $E_{k,cr}$ [J] | $E_k$ [J] | $E_k \geq E_{k,cr}$ ? | $E_k'$ [J] | $V$ [m.s$^{-1}$] | $P_b = P_{b,peak}$ [kN] | $P_t = P_b + P_i$ [kN] | $\Delta P$ [N.s] | $t_p$ [ms] |
|---|---|---|---|---|---|---|---|---|---|---|---|
| 242.1 | 8.02 | 12.5 | 229.6 | 425.9 | YES | 196.3 | 1.8 | 113.1 | 169.2 | 66.3 | 0.78 |

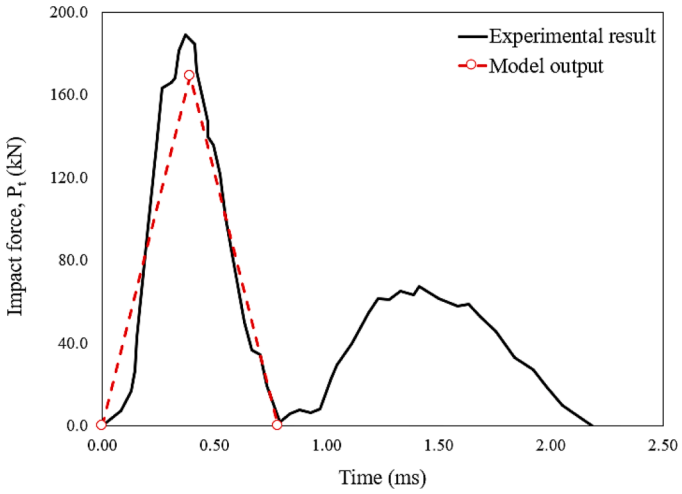


**Fig. B9.** Analytical and experimental (Zhang et al. [23]) impact forces vs time.

## References


[1] Committee A.C.I. Building code requirements for structural concrete ACI 318-19 and commentary 318R–19. Am Concr Inst Aci Comm Farmingt hills, MI, USA 2019.
[2] Lok TS, Zhao PJ, Lu G. Using the split Hopkinson pressure bar to investigate the dynamic behaviour of SFRC. Mag Concr Res 2003;55:183–91.
[3] Su Y, Li J, Wu C, Wu P, Li ZX. Effects of steel fibres on dynamic strength of UHPC. Constr Build Mater 2016;114:708–18.
[4] Wille K, Xu M, El-Tawil S, Naaman AE. Dynamic impact factors of strain hardening UHP-FRC under direct tensile loading at low strain rates. Mater Struct 2016;49:1351–65.
[5] Tran TK, Kim DJ. Investigating direct tensile behavior of high performance fiber reinforced cementitious composites at high strain rates. Cem Concr Res 2013;50:62–73.
[6] Pyo S, El-Tawil S, Naaman AE. Direct tensile behavior of ultra high performance fiber reinforced concrete (UHP-FRC) at high strain rates. Cem Concr Res 2016;88:144–56.
[7] Tran NT, Tran TK, Jeon JK, Park JK, Kim DJ. Fracture energy of ultra-high-performance fiber-reinforced concrete at high strain rates. Cem Concr Res 2016;79:169–84.
[8] Park JK, Kim SW, Kim DJ. Matrix-strength-dependent strain-rate sensitivity of strain-hardening fiber-reinforced cementitious composites under tensile impact. Compos Struct 2017;162:313–24.
[9] Banthia N, Mindess S, Bentur A, Pigeon M. Impact testing of concrete using a drop-weight impact machine. Exp Mech 1989;29:63–9.
[10] Wang N, Mindess S, Ko K. Fibre reinforced concrete beams under impact loading. Cem Concr Res 1996;26:363–76.
[11] Ulzurrun G, Zanuy C. Flexural response of SFRC under impact loading. Constr Build Mater 2017;134:397–411.
[12] Millard SG, Molyneaux TCK, Barnett SJ, Gao X. Dynamic enhancement of blast-resistant ultra high performance fibre-reinforced concrete under flexural and shear loading. Int J Impact Eng 2010;37:405–13.
[13] Zanuy C, Ulzurrún GSD. Rate effects of fiber-reinforced concrete specimens in impact regime. Procedia Eng 2017;193:501–8.
[14] Hao Y, Hao H, Chen G. Experimental investigation of the behaviour of spiral steel fibre reinforced concrete beams subjected to drop-weight impact loads. Mater Struct 2016;49:353–70.
[15] Yoo D-Y, Yoon YS, Banthia N. Flexural response of steel-fiber-reinforced concrete beams: effects of strength, fiber content, and strain-rate. Cem Concr Compos 2015;64:84–92.
[16] Suaris W, Shah SP. Strain-rate effects in fibre-reinforced concrete subjected to impact and impulsive loading. Composites 1982;13:153–9.
[17] Bentur A, Mindess S, Banthia N. The behaviour of concrete under impact loading: experimental procedures and method of analysis. Mater Struct 1986;19:371–8.
[18] Banthia N, Gupta P, Yan C. Impact resistance of fiber reinforced wet-mix shotcrete part 1: beam tests. Mater Struct 1999;32:563–70.
[19] Gopalaratnam VS, Shah SP. Properties of steel fiber reinforced concrete subjected to impact loading. J Proc 1986;83:117–26.
[20] Teng TL, Chu YA, Chang FA, Shen BC, Cheng D-S. Development and validation of numerical model of steel fiber reinforced concrete for high-velocity impact. Comput Mater Sci 2008;42:90–9.
[21] Wang Z, Zhou N, Wang J. Using Hopkinson pressure bar to perform dynamic tensile tests on SFRC at medium strain rates. Mag Concr Res 2012;64:657–64.
[22] Mindess S, Banthia NP, Ritter A, Skalny JP. Crack development in cementitious materials under impact loading. MRS Online Proc Libr 1985;64.
[23] Zhang XX, Abd Elazim AM, Ruiz G, Yu RC. Fracture behaviour of steel fibre-reinforced concrete at a wide range of loading rates. Int J Impact Eng 2014;71:89–96.
[24] Pham TM, Hao H. Prediction of the impact force on reinforced concrete beams from a drop weight. Adv Struct Eng 2016;19:1710–22.
[25] Carta G, Stochino F. Theoretical models to predict the flexural failure of reinforced concrete beams under blast loads. Eng Struct 2013;49:306–15.
[26] Fujikake K, Li B, Soeun S. Impact response of reinforced concrete beam and its analytical evaluation. J Struct Eng 2009;135:938.
[27] Zhao W, Qian J, Jia P. Peak response prediction for RC beams under impact loading. Shock Vib 2019. 2019.
[28] Othman H, Marzouk H, Sherif M. Effects of variations in compressive strength and fibre content on dynamic properties of ultra-high performance fibre-reinforced concrete. Constr Build Mater 2019;195:547–56.
[29] Bakhshi M, Valente IB, Ramezansefat H, Barros JAO, Pereira ENB, Peixinho NRM. Experimental investigation of the effect of high strain rate loading on the flexural behaviour of the steel fibre-reinforced concrete. Fib Symp 2021:604–13. 2021-June.
[30] Banthia N, Mindess S. Impact resistance of steel fiber reinforced concrete. Mater J 1996;93:472–9.
[31] Yazıcı Ş, Arel HŞ, Tabak V. The effects of impact loading on the mechanical properties of the SFRCs. Constr Build Mater 2013;41:68–72.
[32] Yoo D-Y, Banthia N. Impact resistance of fiber-reinforced concrete–a review. Cem Concr Compos 2019;104:103389.
[33] CEB-FIP. Model code 2010. Com Euro-international du bet 2010.
[34] Sujivorakul C. Model of hooked steel fibers reinforced concrete under tension. High Perform Fiber Reinf Cem Compos 2012;6:19–26. Springer.
[35] Barros JAO, Figueiras JA. Flexural behavior of SFRC: testing and modeling. J Mater Civ Eng 1999;11:331–9.
[36] Ou YC, Tsai MS, Liu KY, Chang KC. Compressive behavior of steel-fiber-reinforced concrete with a high reinforcing index. J Mater Civ Eng 2012;24:207–15.
[37] Wang ZL, Liu YS, Shen RF. Stress–strain relationship of steel fiber-reinforced concrete under dynamic compression. Constr Build Mater 2008;22:811–9.
[38] de Oliveira Júnior LÁ, S Borges VE dos, Danin AR, Machado DVR, Araújo D de L, El Debs MK, et al. Stress-strain curves for steel fiber-reinforced concrete in compression. Matéria (Rio Janeiro) 2010;15:260–6.
[39] Malvar LJ, Ross CA. Review of strain rate effects for concrete in tension. ACI Mater J 1998;95:735–9.
[40] CEB-FIP. Design code 1990. Com Euro Int Du Bet 1990:51–9.
[41] Bažant ZP, Oh BH. Crack band theory for fracture of concrete. Matériaux Constr 1983;16:155–77.
[42] Barros JAO, Sena-Cruz J. Fracture energy of steel fiber-reinforced concrete. Mech Compos Mater Struct 2001;8:29–45.
[43] Tarifa M, Poveda E, Cunha VMCF, Barros JAO. Effect of the displacement rate and inclination angle in steel fiber pullout tests. Int J Fract 2020;223:109–22.
[44] Poveda E, Yu RC, Tarifa M, Ruiz G, Cunha VMCF, Barros JAO. Rate effect in inclined fibre pull-out for smooth and hooked-end fibres: a numerical study. Int J Fract 2020;223:135–49.
[45] Da Silva CAN, Ciambella J, Barros JAO, Costa IG. Analytical bond model for general type of reinforcements of finite embedment length in cracked cement based materials. Int J Solids Struct 2019;167:36–47.
[46] Ramezansefat H, Barros J, Rezazadeh M. A model for the simultaneous prediction of the flexural and shear deflections of statically determinate and indeterminate reinforced concrete structures. Struct Concr 2017;18:618–33.
[47] Gere J.M., Timoshenko S.P. Mechanics of materials, 3rd SI edition, 1991 n.d.
[48] Elsaigh WA, Robberts JM, Kearsley EP. Modelling non-linear behaviour of steel fibre reinforced concrete. In: 6th Int. RILEM Symp. Fibre Reinf. Concr. RILEM Publications SARL; 2004. p. 837–46.
[49] Barragan B, Gettu R, Agullo L, Zerbino R. Shear failure of steel fiber-reinforced concrete based on push-off tests. ACI Mater J 2006;103:251.